Turbulence Modeling of Torsional Couette Flows

Sofia Haddadi, Sébastien Poncet

Hindawi Publishing Corporation
International Journal of Rotating Machinery
Volume 2008, Article ID 635138, 27 pages
doi:10.1155/2008/635138

Research Article

Turbulence Modeling of Torsional Couette Flows

Sofia Haddadi and Sébastien Poncet

Laboratoire M2P2, UMR 6181, CNRS, Universités d'Aix-Marseille, IMT la Jetée, Technopôle Château-Gombert, 38 rue F. Joliot-Curie, 13451 Marseille Cédex 20, France

Correspondence should be addressed to Sébastien Poncet, poncet@l3m.univ-mrs.fr

Received 7 May 2008; Revised 2 September 2008; Accepted 2 October 2008

Recommended by Osamu Nozaki

The present study considers the numerical modeling of the turbulent flow inside a rotor-stator cavity subjected or not to a superimposed throughflow. Extensive numerical predictions based on one-point statistical modeling using a low Reynolds number second-order full stress transport closure (RSM model) are performed mainly in the case of turbulent flows with merged boundary layers known as turbulent torsional Couette flows and belonging to regime III of Daily and Nece (1960). The RSM model has already shown its capability of predicting accurately the mean and turbulent fields in various rotating disk configurations (Poncet, 2005; Poncet et al., 2005, 2007, 2008). For the first time, a detailed mapping of the hydrodynamic flow over a wide range of rotational Reynolds numbers ($1.8 \times 10^5 \leq \mathrm{Re} \leq 10^7$), aspect ratios of the cavity ($0.02 \leq G \leq 0.05$), and flow rate coefficients ($-10^4 \leq C_w \leq 10^4$) is here provided in the turbulent torsional Couette flow regime.

1. INTRODUCTION

Enclosed rotating disks simulate conditions found in a large variety of rotating machinery, including hard disk drives, centrifugal pumps, air cycle machines, and gas turbines. The first sets of extensive and detailed measurements of the hydrodynamic flow in a rotor-stator cavity have been performed by Daily and Nece [1], who proposed also a comprehensive theoretical analysis of rotor-stator flows. They pointed out the existence of four basic flow regimes, whose approximate domains are presented in Figure 1, according to a combination of two parameters: the rotational Reynolds number $\mathrm{Re} = \Omega b^2/\nu$ based on the outer radius b of the rotating disk and to the aspect ratio $G = h/b$ of the cavity, with h the interdisk spacing. The four regimes are denoted as follows.

(i) Regime I: laminar flow with merged boundary layers.

(ii) Regime II: laminar flow with unmerged boundary layers.

(iii) Regime III: turbulent flow with merged boundary layers.

(iv) Regime IV: turbulent flow with unmerged boundary layers.

The physics of turbulent flows with unmerged boundary layers (IV), known as turbulent Batchelor flows, has already been widely addressed both experimentally and numerically [2–4]. The reader is also referred to the experimental work of Schouveiler et al. [5] for details about the transition between regimes II and IV and between regimes I and III. The present work is mainly focused on the regime III of Daily and Nece [1], corresponding to turbulent torsional Couette flows with merged boundary layers (see Figure 1).

For example, at $\mathrm{Re} = 10^7$, Daily and Nece [1] estimate that the transition between the regimes IV and III occurs for $G = 0.0196$. It means that, for a typical rotating disk radius of 250 mm [3], the interdisk spacing should be smaller than 4.9 mm to ensure merged boundary layers. Because of the complexity of making accurate flow measurements in such close clearance, there are relatively few experimental works devoted to this flow regime. A brief review of the works focused on regime III until 1989 is proposed in the detailed monograph of Owen and Rogers [6]. The main experimental investigation to our knowledge is the one of Daily et al. [7], who performed mean velocity, torque, and pressure measurements, for $G = 0.0138$ and two Reynolds numbers $\mathrm{Re} = 2.95-6.9\times10^5$. For this set of parameters, they clearly obtained merged boundary layers. They investigated

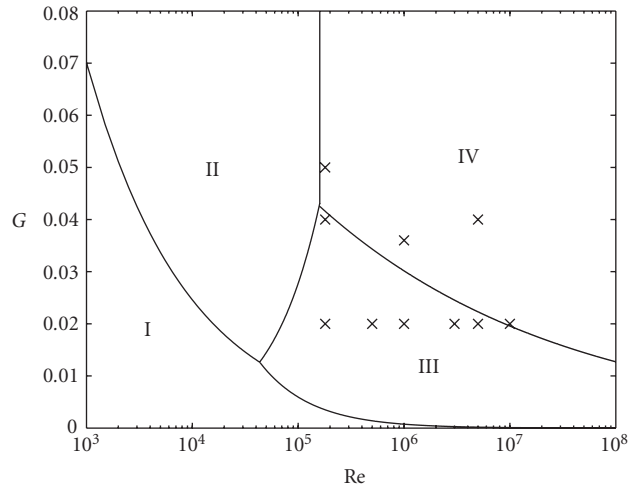

Figure 1: Diagram of the four-flow regimes according to Daily and Nece [1] with the cases considered here (cross-symbols).

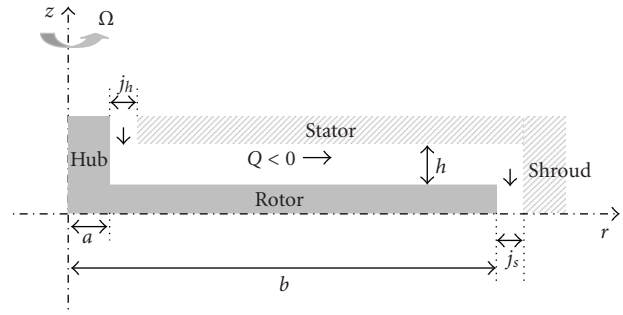

Figure 2: Schematic representation of the rotor-stator configuration and notations.

also the influence of a radial outward throughflow on the flow structure. Phadke and Owen [8] studied, using flow visualizations and pressure measurements, the effect of seven shroud geometries on the ingress of external fluid into the rotor-stator cavity for a large range of flow control parameters including the torsional Couette flow regime.

The difficulty to acquire accurate measurements in such close clearances has reduced the development of advanced numerical codes adapted to these geometries. Cooper and Reshotko [9] proposed a scalar effective viscosity technique to calculate the flow in a rotor-stator cavity of infinite radius for both close and large clearances. It provided qualitatively good results compared to the experimental data of Daily and Nece [1] obtained without throughflow. Iacovides and Theofanopoulos [10] used an algebraic modeling of the Reynolds stress tensor in the fully developed turbulence area and a mixing length hypothesis near the wall. It provided satisfactory results compared to simpler models in the case of a rotor-stator flow with and without throughflow but some discrepancies remained and the authors concluded that no single form of their models was satisfactory for all rotating disk configurations considered. Poncet et al. [2, 3, 11] compared pressure and velocity measurements with numerical predictions based on an improved version of the Reynolds stress modeling of Elena and Schiestel [12] for centripetal and centrifugal throughflows mostly in the case of large aspect ratio cavities. All the comparisons were in good agreement for both the mean and turbulent fields. Andersson and Lygren [13] performed some large-eddy simulations of enclosed rotor-stator flows (the cavity was assumed to be periodic in both the tangential and radial directions) for both the wide and narrow gap cases. They obtained a turbulent torsional Couette flow for $G = 0.01$ and $\mathrm{Re} = 1.6 \times 10^6$. At that time, three-dimensional accurate simulations (DNS or LES) are still limited to relatively low Reynolds numbers and most of all to idealized enclosed cavities without throughflow. Moreover, they require several millions of mesh points and excessive calculation times preventing from performing a parametric study in such a complex configuration. Finally, as there is no experimental or numerical evidence at that time that three-dimensional unsteady structures exist at very high rotation rates in the case of turbulent torsional Couette flows (contrary to turbulent Batchelor flows for which Czarny et al. [14] have observed precessing 3D vortexes), the RSM model used by Poncet et al. [2, 3] seems to be a valuable tool to describe such complex flows and to perform a parametric study of merged turbulent flows with strong axial throughflows.

The present paper is devoted to the modeling of turbulent flows in a rotor-stator system of small aspect ratio (regime III [1]) when an axial throughflow is superimposed on the rotating fluid. The basic flow belongs to the torsional Couette type family: the two boundary layers are merged. Besides their industrial applications in turbomachinery, these flows offer a relatively simple configuration to study the influence of both rotation and shear on turbulence. The aim of this work is so to provide a better understanding of the flow dynamics in such complex flows and to quantify the influence of the flow control parameters: the Reynolds number, the flowrate coefficient, and especially the aspect ratio of the cavity. The paper is divided as follows: Section 2 is devoted to the statistical modeling including the description of the geometrical configuration, the presentation of the numerical modeling, and the validation of the RSM model against experimental data [1]. In Section 3, the effect of both the Reynolds number and the aspect ratio of the cavity on the mean and turbulent fields in the case of a closed system (without throughflow) is discussed. The influence of an inward and an outward axial throughflow on the flow structures and on turbulence is presented in Section 4 for a given aspect ratio before concluding in Section 5.

2. STATISTICAL MODELING

2.1. Geometrical configuration

The cavity sketched in Figure 2 is composed of a smooth stationary disk (the stator) and a smooth rotating disk (the rotor). A fixed shroud encloses the cavity. The rotor and the central hub attached to it rotate at the uniform angular velocity Ω.

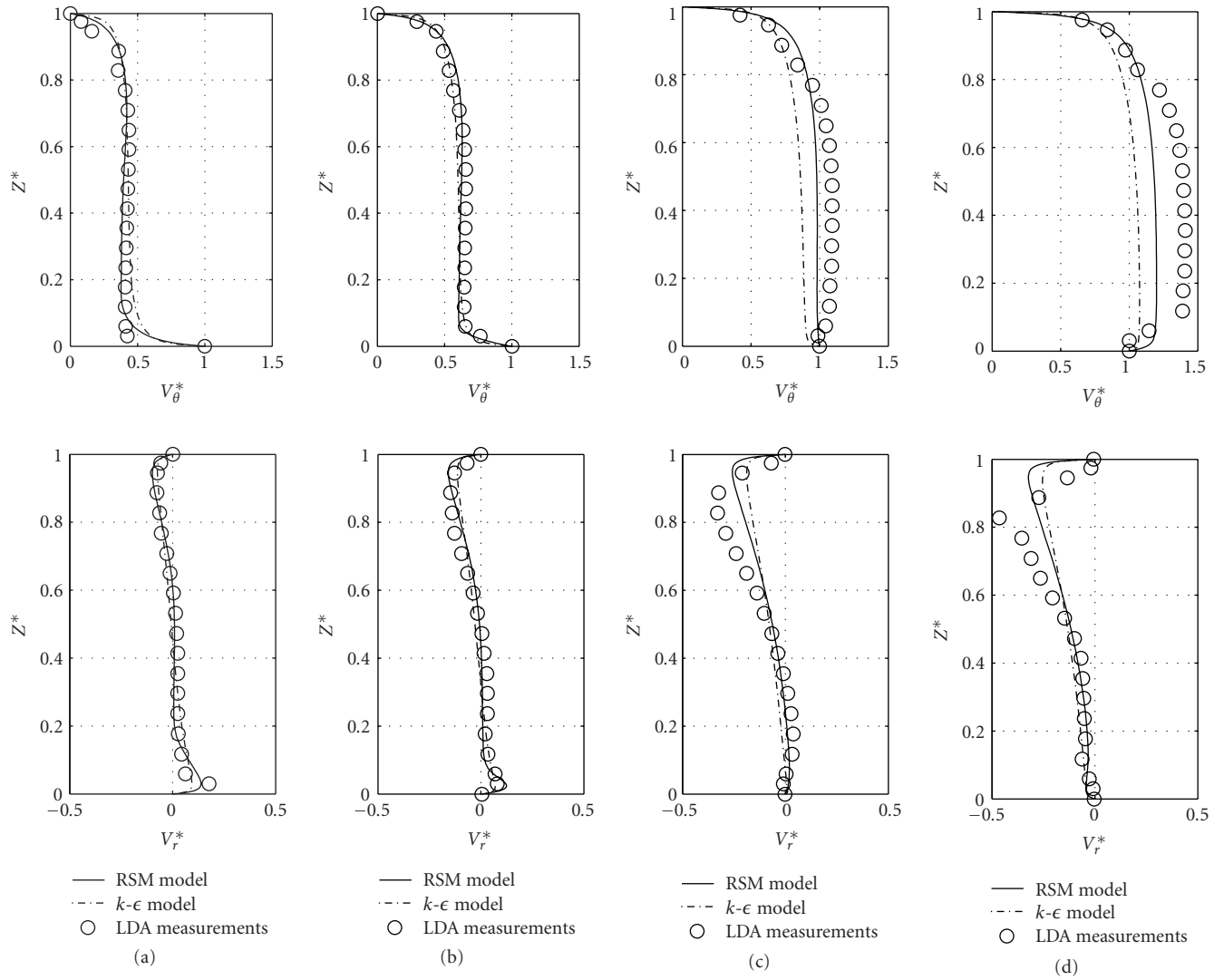

FIGURE 3: Axial profiles of two mean velocity components at $r^* = 0.56$ for $G = 0.036$ and $\mathrm{Re} = 10^6$ with or without a centripetal superimposed throughflow: (a) $C_w = 0$, (b) $C_w = 1976$, (c) $C_w = 5929$, (d) $C_w = 9881$. Comparisons between the present RSM model $(-)$, the k-ϵ model $(-\cdot-)$, and LDA measurements $(\circ)$.

The mean flow is mainly governed by four flow control parameters: the aspect ratio G, and the curvature parameter R_m of the cavity, the rotational Reynolds number Re based on the outer radius of the rotating disk, and the flow rate coefficient C_w defined as follows:

(i) $0.02 \le G = h/b \le 0.05$,

(ii) $R_m = (b + a)/(b - a) = 1.33$,

(iii) $1.8 \times 10^5 \le \mathrm{Re} = \Omega b^2/\nu \le 10^7$,

(iv) $-10^4 \le C_w = Q/(\nu b) \le 10^4$,

where ν is the fluid kinematic viscosity, a, b the radii of the hub and of the rotating disk, respectively, h the interdisk spacing, and Q the superimposed throughflow. Note that Q is a volume flow rate. $C_w = 0$ corresponds to a closed cavity. $C_w > 0$ (resp., < 0) denotes the case where a centripetal (resp., centrifugal) throughflow is superimposed. The dimensionless values of the radial gaps j_h/b between the hub and the stator and j_s/b between the rotor and the shroud are fixed to 0.076 and 0.012, respectively.

2.2. The differential Reynolds stress model (RSM)

The flow studied here presents several complexities (high rotation rate, imposed throughflow, wall effects, and transition zones), which are severe conditions for turbulence modeling methods [15, 16]. Our approach is based on one-point statistical modeling using a low Reynolds number second-order full stress transport closure derived from the Launder and Tselepidakis [17] model and sensitized to rotation effects [12, 18]. Previous works [3, 12, 19] have shown that this level of closure was adequate in such

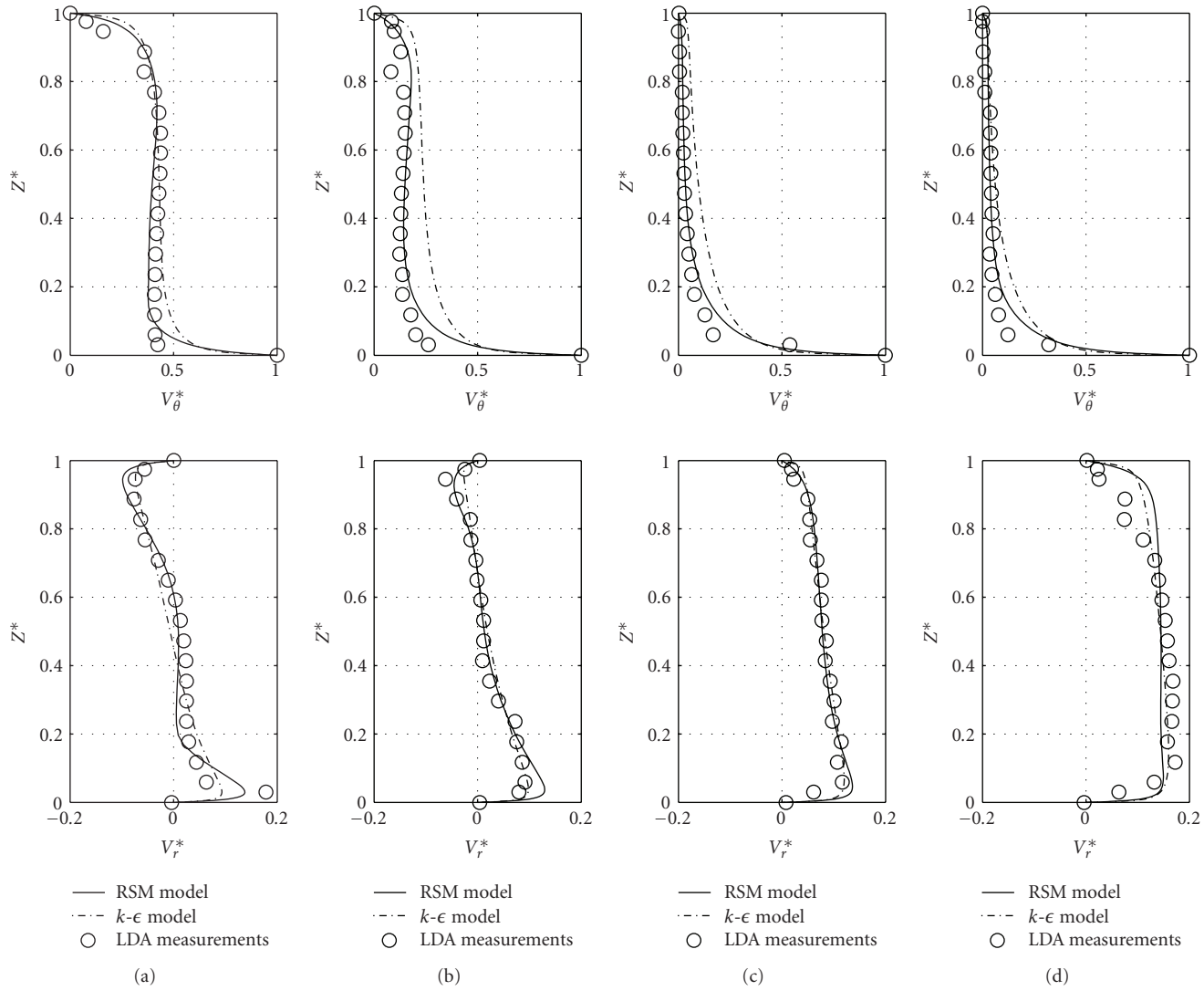

FIGURE 4: Axial profiles of two mean velocity components at $r^* = 0.56$ for $G = 0.036$ and $\mathrm{Re} = 10^6$ with or without a centrifugal superimposed throughflow: (a) $C_w = 0$, (b) $C_w = -1976$, (c) $C_w = -5929$, (d) $C_w = -9881$. Comparisons between the present RSM model ($-$), the k-ϵ model ($-\cdot-$), and LDA measurements ($\circ$).

flow configurations, while the usual k-ϵ model, which is blind to any rotation effect presents serious deficiencies. This approach allows for a detailed description of near-wall turbulence and is free from any eddy viscosity hypothesis. The general equation for the Reynolds stress tensor R_{ij} can be written as

$$\frac{dR_{ij}}{dt} = P_{ij} + D_{ij} + \Phi_{ij} - \epsilon_{ij} + T_{ij}, \tag{1}$$

where P_{ij}, D_{ij}, Φ_{ij}, ϵ_{ij}, and T_{ij}, respectively, denote the production, diffusion, pressure-strain correlation, dissipation, and extra terms.

The diffusion term D_{ij} is split into two parts: a turbulent diffusion D_{ij}^T, which is interpreted as the diffusion due to both velocity and pressure fluctuations [20] and a viscous diffusion D_{ij}^ν, which cannot be neglected in the low Reynolds number region:

$$D_{ij}^T = \left(0.22\frac{k}{\varepsilon}R_{kl}R_{ij,l}\right)_{,k},$$
$$D_{ij}^\nu = -\nu R_{ij,kk}. \tag{2}$$

In a classical way, the pressure-strain correlation term Φ_{ij} can be decomposed as follows:

$$\Phi_{ij} = \Phi_{ij}^{(1)} + \Phi_{ij}^{(2)} + \Phi_{ij}^{(w)}, \tag{3}$$

where $\Phi_{ij}^{(1)}$ is interpreted as a slow nonlinear return to isotropy and is modeled as a quadratic development in the stress anisotropy tensor a_{ij}, with coefficients sensitized to the invariants of anisotropy. This term is damped near the wall

$$\Phi_{ij}^{(1)} = -\left(\tilde{c}_1 a_{ij} + c_1'\left(a_{ik}a_{kj} - \frac{1}{3}A_2\delta_{ij}\right)\right)\varepsilon, \tag{4}$$

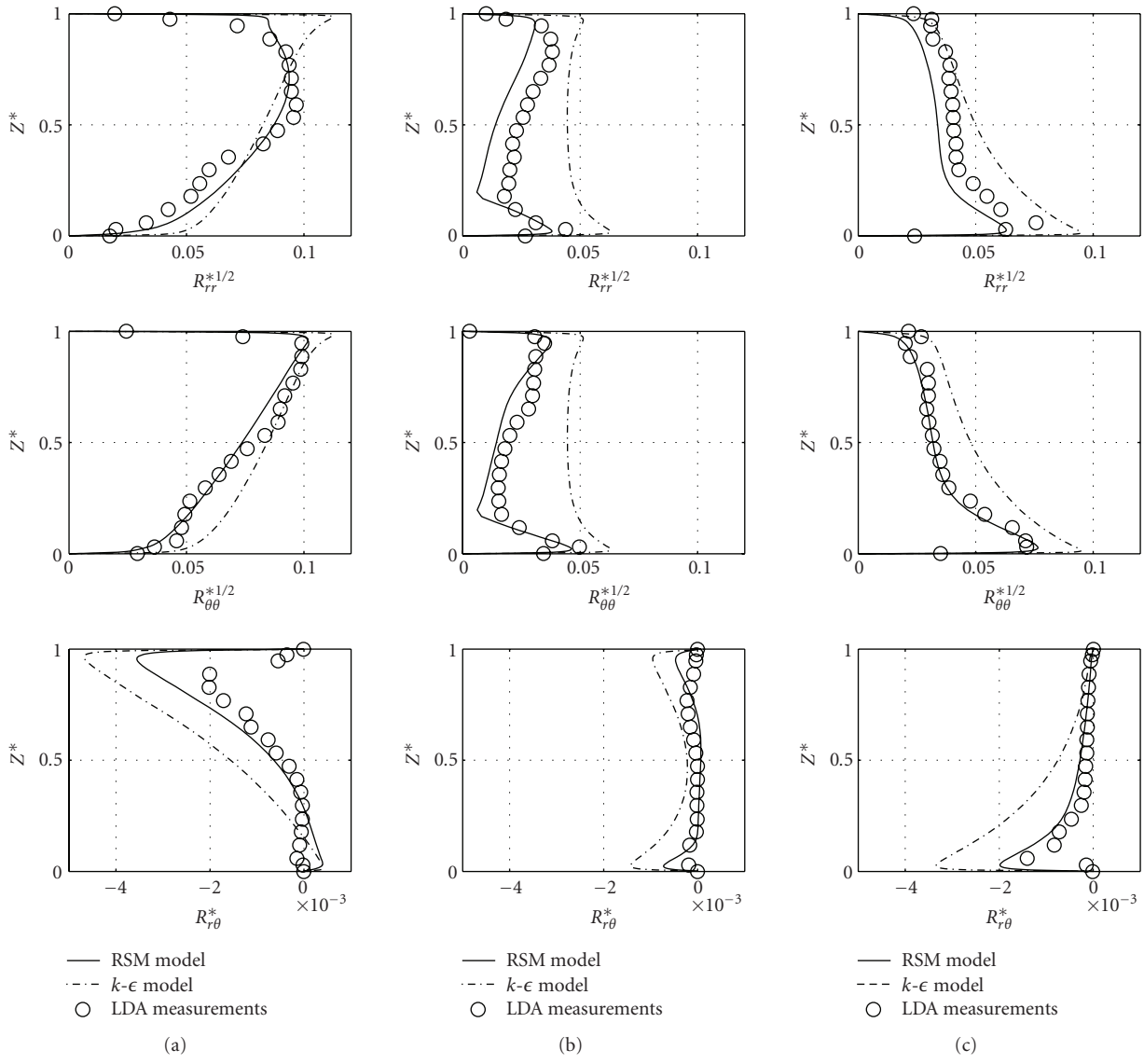

FIGURE 5: Axial profiles of three Reynolds stress tensor components at $r^* = 0.56$ for $G = 0.036$ and $\mathrm{Re} = 10^6$: (a) $C_w = 9881$, (b) $C_w = 0$, (c) $C_w = -9881$. Comparisons between the present RSM model (−), the k-ϵ model (−·−), and LDA measurements (∘).

where a_{ij} denotes the stress anisotropy tensor and $\widetilde{c}_1$ and c_1' are two functions deduced from Craft's high-Reynolds number proposals [21] adapted for confined flows

$$a_{ij} = \frac{R_{ij}}{k} - \frac{2}{3}\delta_{ij},$$
$$\widetilde{c}_1 = \left(3.1\sqrt{AA_2} + 1\right)\left(1 - e^{-\mathrm{Re}_t^2/40}\right), \tag{5}$$
$$c_1' = 3.72\sqrt{AA_2}\left(1 - e^{-\mathrm{Re}_t^2/40}\right),$$

where $A = 1 - 9/8(A_2 - A_3)$ is the Lumley's flatness parameter with A_2 and A_3 as the second and third invariants of the anisotropy tensor. $\mathrm{Re}_t = k^2/(\nu\varepsilon)$ is the turbulence Reynolds number.

The linear rapid part $\Phi_{ij}^{(2)}$ includes cubic terms. It can be written as

$$\begin{aligned}\Phi_{ij}^{(2)} = {} & -0.6\left(P_{ij} - \frac{1}{3}P_{kk}\delta_{ij}\right) + 0.3\varepsilon a_{ij}\frac{P_{kk}}{\varepsilon} \\ & - 0.2\left[\frac{R_{kj}R_{li}}{k}\left(V_{k,l} + V_{l,k}\right) - \frac{R_{lk}}{k}\left(R_{ik}\left(V_{j,l} + \epsilon_{jml}\Omega_m\right)\right.\right. \\ & \left.\left. + R_{jk}\left(V_{i,l} + \epsilon_{iml}\Omega_m\right)\right)\right] \\ & - \min(0.6, A)\left(A_2\left(P_{ij} - D_{ij}\right) + 3a_{mi}a_{nj}\left(P_{mn} - D_{mn}\right)\right),\end{aligned} \tag{6}$$

with $P_{ij} = -R_{ij}V_{j,k} - R_{jk}V_{i,k}$ and $D_{ij} = -R_{ik}V_{k,j} - R_{jk}V_{k,i}$.

Since the slow part of the pressure-strain correlation is already damped near the wall, a wall correction $\Phi_{ij}^{(w)}$ is only

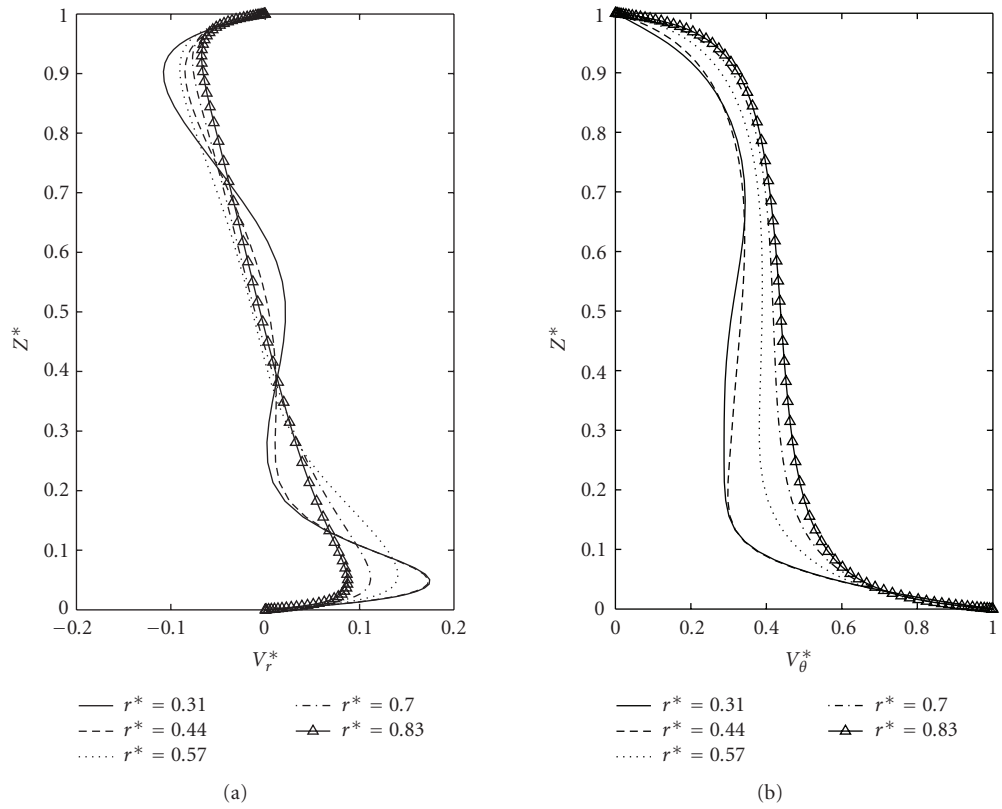

Figure 6: Axial profiles of the mean radial and tangential velocity components for $\mathrm{Re} = 10^6$ and $G = 0.02$ at different radial locations r^*.

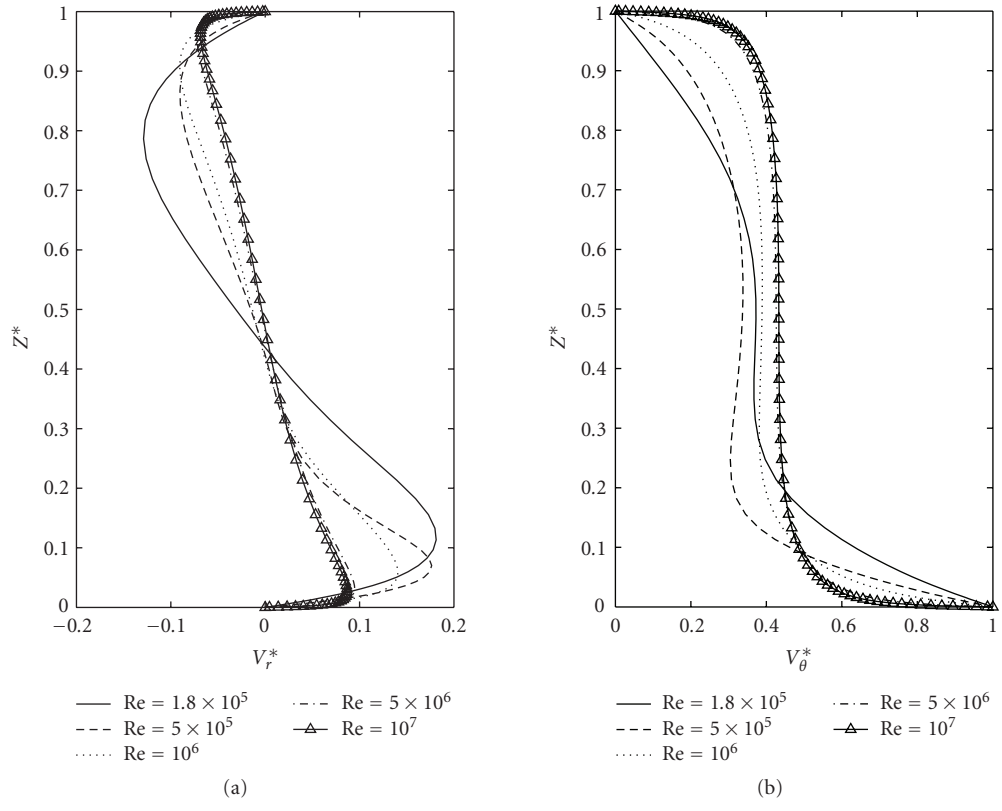

Figure 7: Axial profiles of two mean velocity components at $r^* = 0.57$ for $G = 0.02$ and different Reynolds numbers.

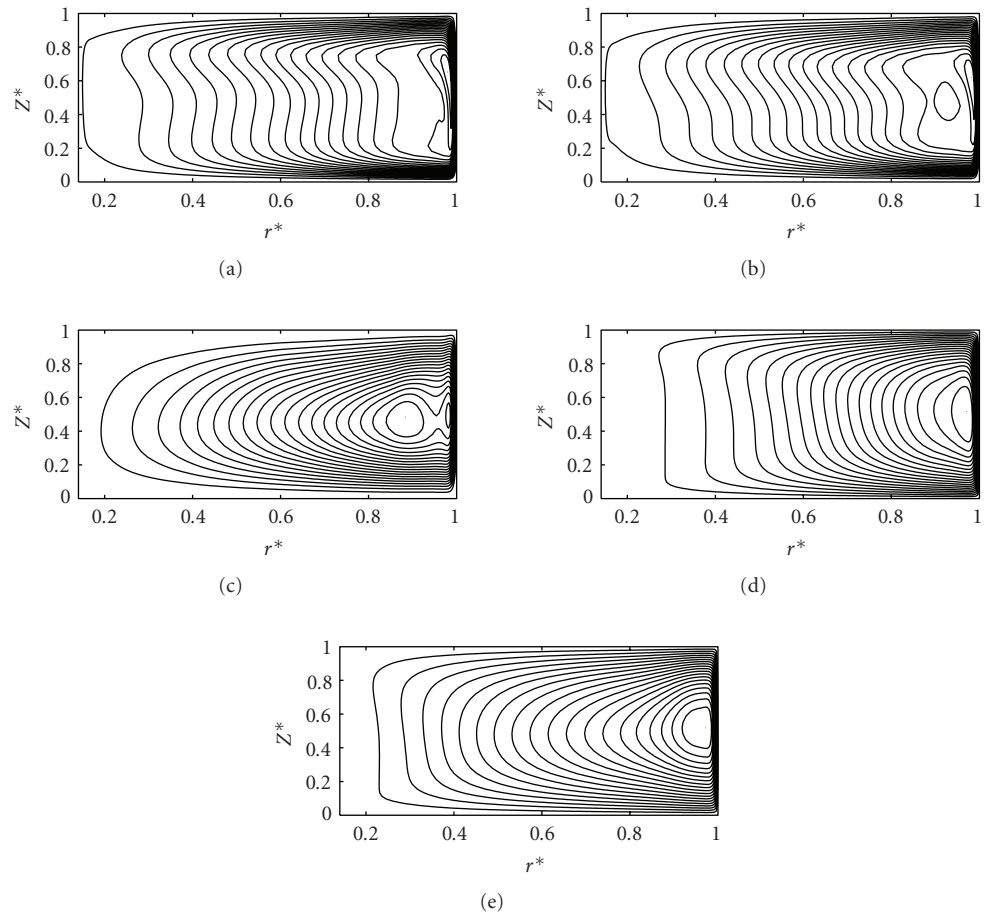

FIGURE 8: Influence of the aspect ratio on the streamline patterns $\Psi^* = \Psi/(\Omega h^2)$ (20 contours) for various sets of flow parameters (Re, G): (a) $(1.8 \times 10^5, 0.05)$, $-0.03 \le \Psi^* \le 5.96$; (b) $(1.8 \times 10^5, 0.04)$, $-0.05 \le \Psi^* \le 10.8$; (c) $(1.8 \times 10^5, 0.02)$, $-0.31 \le \Psi^* \le 76.89$; (d) $(5 \times 10^6, 0.04)$, $-0.04 \le \Psi^* \le 8.32$; (e) $(5 \times 10^6, 0.02)$, $-0.32 \le \Psi^* \le 36.92$.

applied to the rapid part. The form retained here is the one proposed by Gibson and Launder [22] with a strongly reduced numerical coefficient. Moreover the classical length scale $k^{3/2}\varepsilon^{-1}$ is replaced by $k/\varepsilon(R_{ij}n_in_j)^{1/2}$ which is the length scale of the fluctuations normal to the wall

$$\Phi_{ij}^{(w)} = 0.2\Big[(\Phi_{km}^{(2)} + \Phi_{km}^{(R)})n_kn_m\delta_{ij} - \frac{3}{2}(\Phi_{ik}^{(2)} + \Phi_{ik}^{(R)})n_kn_j - \frac{3}{2}(\Phi_{kj}^{(2)} + \Phi_{kj}^{(R)})n_in_k\Big]\frac{k\sqrt{R_{pq}n_pn_q}}{\varepsilon y}, \tag{7}$$

where y is evaluated by the minimal distance of the current point from the four walls.

The viscous dissipation tensor ε_{ij} has been modeled in order to conform with the wall limits obtained from Taylor series expansions of the fluctuating velocities [23]

$$\varepsilon_{ij} = f_A\varepsilon_{ij}^* + (1 - f_A)\left(f_s\frac{\varepsilon R_{ij}}{k} + \frac{2}{3}(1 - f_s)\varepsilon\delta_{ij}\right), \tag{8}$$

with f_A, f_s and ε_{ij}^* defined as

$$f_A = e^{-20A^2}e^{-\mathrm{Re}_t^2/20},$$
$$f_s = e^{-\mathrm{Re}_t^2/40},$$
$$\varepsilon_{ij}^* = \frac{(R_{ij} + R_{ik}n_jn_k + R_{jk}n_in_k + R_{kl}n_kn_ln_in_j)}{(k/\varepsilon)(1 + (3/2)(R_{pq}/k)n_pn_q)}. \tag{9}$$

The extra term $T_{ij} = \Phi_{ij}^{(R)} + B_{ij} + D_{ij}^R + J_{ij}$ accounts for implicit effects of the rotation on the turbulence field. $\Phi_{ij}^{(R)}$, which is a linear contribution in the pressure-strain correlation, is a function of the dimensionality tensor, which represents the spatial properties of the turbulent structures as the elongation of the vortices. B_{ij} is a spectral jamming term acting only in the case of strong rotation. The inhomogeneous diffusion term D_{ij}^R slows down the bidimensionalization of the flow close to the walls. Finally, J_{ij} denotes the inverse flux due to rotation, which impedes the energy cascade. All these terms are detailed in [11, 19]. They allowed some improvements of the numerical predictions of the previous RSM models [12].

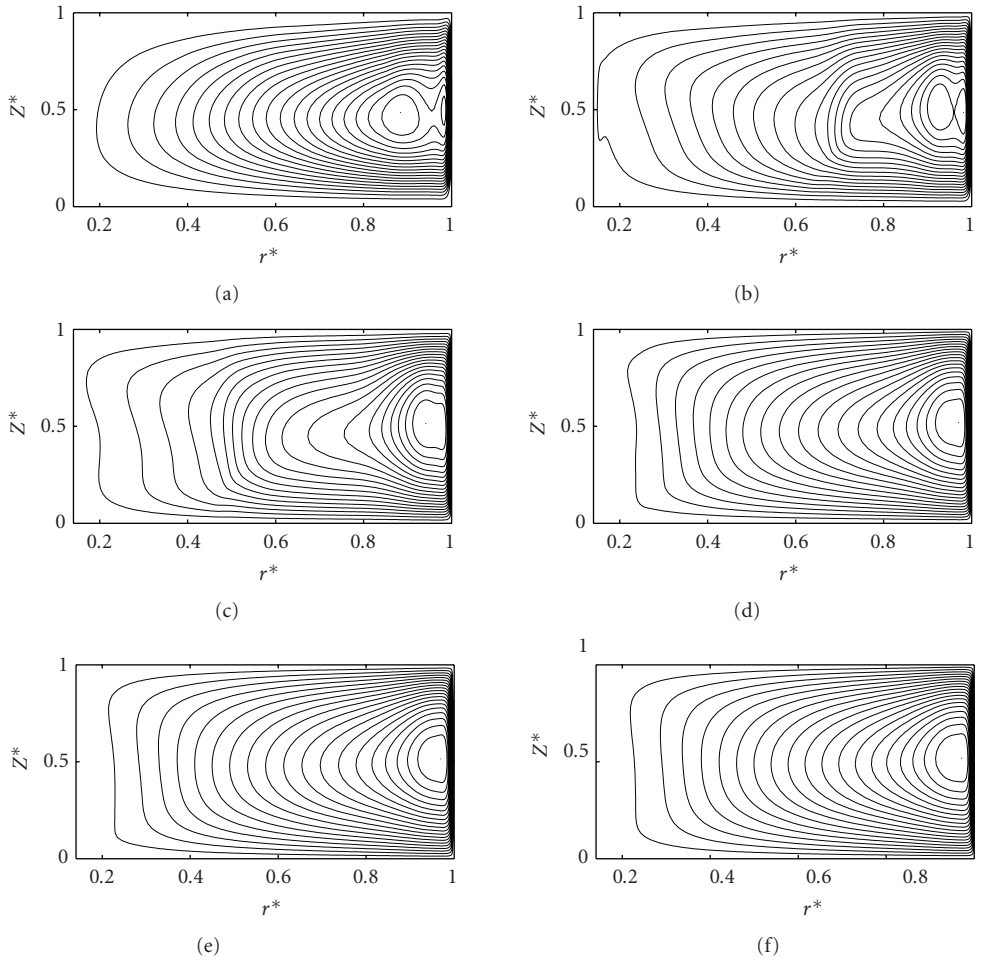

Figure 9: Influence of the Reynolds number on the streamline patterns Ψ^* (20 contours) for $G = 0.02$ and six values of Re: (a) 1.8×10^5, $-0.31 \le \Psi^* \le 76.89$; (b) 5×10^5, $-0.66 \le \Psi^* \le 60.59$; (c) 10^6, $-0.63 \le \Psi^* \le 48.19$; (d) 3×10^6, $-0.41 \le \Psi^* \le 39.16$; (e) 5×10^6, $-0.32 \le \Psi^* \le 36.92$; (f) 10^7, $-0.23 \le \Psi^* \le 34.38$.

Below is the proposal of Launder and Tselepidakis [17] for the dissipation rate equation ε

$$\frac{d\varepsilon}{dt} = -c_{\varepsilon_1}\frac{\varepsilon}{k}R_{ij}V_{i,j} - c_{\varepsilon_2}f_\varepsilon\frac{\widetilde{\varepsilon}\varepsilon}{k} + \left(c_\varepsilon\frac{k}{\varepsilon}R_{ij}\varepsilon_{,j} + \nu\varepsilon_{,i}\right)_{,i} + c_{\varepsilon_3}\nu\frac{k}{\varepsilon}R_{jk}V_{i,jl}V_{i,kl} + \left(c_{\varepsilon_4}\nu\frac{\widetilde{\varepsilon}}{k}k_{,i}\right)_{,i}, \quad (10)$$

where $\widetilde{\varepsilon}$ is the isotropic part of the dissipation rate $\widetilde{\varepsilon} = \varepsilon - 2\nu k_{,i}^{1/2}k_{,i}^{1/2}$. $c_{\varepsilon_1} = 1$, $c_{\varepsilon_2} = 1.92$, $c_\varepsilon = 0.15$, $c_{\varepsilon_3} = 2$, and $c_{\varepsilon_4} = 0.92$ are four empirical constants and f_ε is defined by $f_\varepsilon = 1/(1 + 0.63\sqrt{AA_2})$. Note that all these numerical constants are used by the scientific community and their values have been determined once and for all by numerical optimization or experiments (decay of isotropic turbulence behind a grid, turbulent boundary layer, and so forth). The reader can refer to the work of Elena [19] for more details. No numerical optimization has been performed in the present study.

The turbulence kinetic energy equation is redundant in an RSM model but it is however still solved numerically in order to get faster convergence

$$\frac{dk}{dt} = -R_{ij}V_{i,j} - \varepsilon + \frac{T_{jj}}{2} + 0.22\left(\frac{k}{\varepsilon}R_{ij}k_{,j} + \nu k_{,i}\right)_{,i}. \quad (11)$$

It is verified after convergence that k is exactly $0.5R_{jj}$.

2.3. Numerical method

The computational procedure is based on a finite volume method using staggered grids for mean velocity components with axisymmetry hypothesis in the mean. The computer code is steady elliptic and the numerical solution proceeds iteratively. Elena [19] and then Poncet et al. [2, 3] proved that a 140×80 mesh in the (r, z) frame is sufficient in most cases to get grid-independent solutions. Nevertheless, a more refined mesh 200×80 in the radial direction has been used in the present case to take into account the narrow gap cases. To check the grid independence of

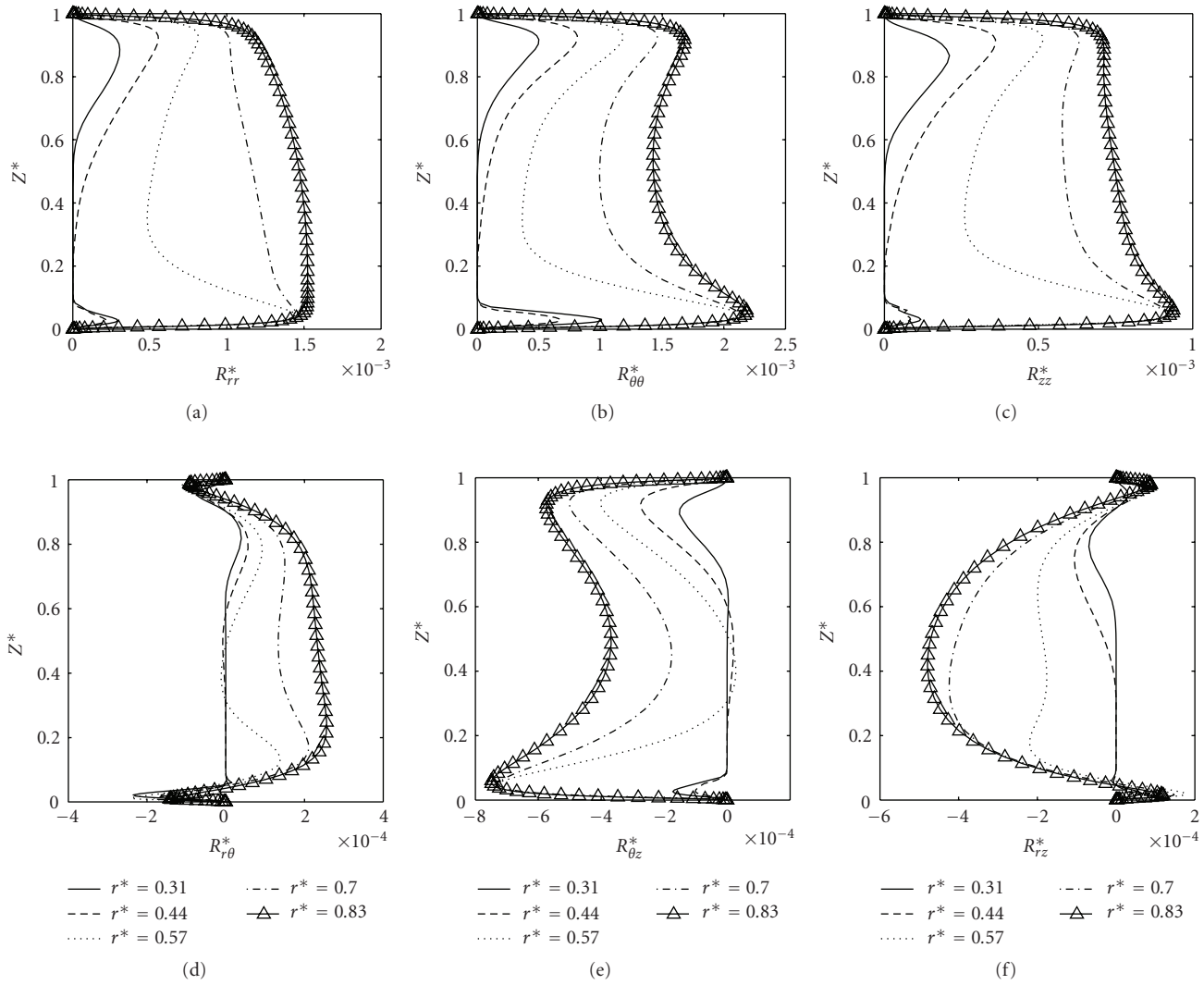

Figure 10: Axial profiles of the six Reynolds stress tensor components for $\mathrm{Re} = 10^6$ and $G = 0.02$ at different radial locations r^*.

the solution, some crucial quantities for turbulent rotor-stator flows have been considered: the extrema of the mean radial velocity component along the two disks and the mean tangential velocity component at midplane for the mean field, and the maximum of the turbulence kinetic energy in the whole cavity for the turbulent field. Table 1 shows that the 200×80 mesh provides the best arrangement between accuracy and calculation time compared to the three other meshes considered. For this grid, the size of the first mesh is $\Delta_1 r = 1.677 \times 10^{-4} h$ and $\Delta_1 z = 1.532 \times 10^{-4} h$ in the radial and axial directions, respectively.

It is also verified that the grid is sufficiently refined close the disks to describe accurately the viscous sublayers. For example, the wall coordinate $z^+ = \Delta_1 z u^*/\nu$ (u^* the friction velocity at the wall and $\Delta_1 z$ the size of the first mesh in the axial direction) remains below 0.1 along both disks and for the whole radial extent for $G = 0.04$, $\mathrm{Re} = 1.8 \times 10^5$, and $C_w = 0$. It is quite below the classical value $z^+ = 1$, for which the viscous sublayer is described by 5 mesh points.

Table 1: Influence of the mesh grid on the mean and turbulent fields for $G = 0.02$, $\mathrm{Re} = 10^6$, and $C_w = 0$. Comparisons with the 200×80 mesh which is chosen as the reference mesh grid.

Difference with the 200×80 mesh	250×80	300×80	250×100
Mean field	0.5%	0.6%	0.5%
Turbulent field	1.9%	2.1%	2%

About 20 000 iterations (about 7 hours on the M2P2 cluster composed of 2 xeon quadcore 3 GHz) are necessary to obtain the numerical convergence of the calculation. In order to overcome stability problems, several stabilizing techniques have been introduced in the numerical procedure, such as those proposed by Huang and Leschziner [24]. Also, the stress component equations are solved using matrix block tridiagonal solution to enhance stability using non-staggered grids.

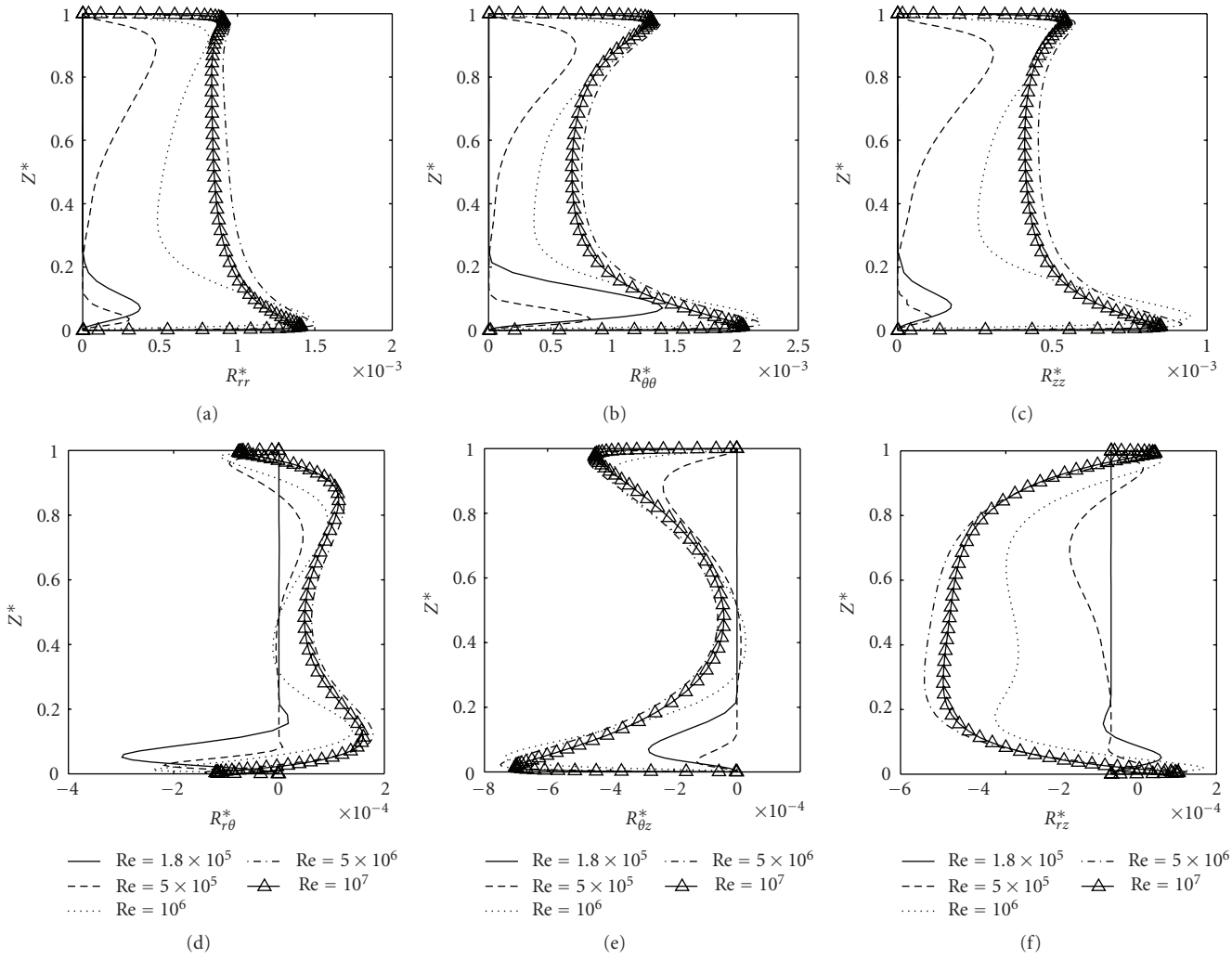

Figure 11: Axial profiles of the six Reynolds stress tensor components at $r^* = 0.57$ for $G = 0.02$ and different Reynolds numbers.

2.4. Boundary conditions

At the wall, all the variables are set to zero except for the tangential velocity V_θ, which is set to Ωr on rotating walls and zero on stationary walls. At the inlet, V_θ is supposed to vary linearly from zero on the stationary wall up to Ωr on the rotating wall. We recall that the inlet is close to the axis of the cavity when a centrifugal throughflow is superimposed, whereas it is located at the periphery in the case of a centripetal throughflow. When a throughflow (centrifugal or centripetal) is enforced, a parabolic profile is then imposed for the axial velocity V_z at the inlet, with a given low level of turbulence intensity. The value of the turbulence kinetic energy imposed at the inlet has only a very weak influence (less than 0.1%) on the mean and turbulent fields [11]. In the outflow section, the pressure is fixed, whereas the derivatives for all the other independent quantities are set to zero if the fluid leaves the cavity, and fixed external values are imposed if the fluid re-enters the cavity. In this case, the continuity equation is used to determine this inward or outward velocity component. The boundary condition is then of a mixed type and a special technique is used to enhance stability [11]. Note that the flow in the similarity area is practically not sensitive to the shape of profiles of tangential and axial velocity components or to the intensity level imposed at the inlet [11]. Moreover, all these choices are justified by the wish to have a model as universal as possible.

In the following, all the quantities have been normalized as follows: $z^* = z/h$, $r^* = r/(b + j_s)$, $V_i^* = \overline{V_i}/(\Omega r)$, and $R_{ij}^* = \overline{v_i' v_j'}/(\Omega r)^2$ with $i, j = (r, \theta, z)$.

2.5. Validation of the RSM model

The predictions of the RSM model have already been widely validated in various rotating disk configurations: turbulent Batchelor flows in a rotor-stator cavity (regime IV of [1]) with or without an imposed axial throughflow [2, 3], with heat transfer effects [25], turbulent Stewartson flows in an open cavity with throughflow [2, 3], and turbulent Von Kármán flow between counterrotating disks equipped or not with straight blades [26]. Nevertheless, to show the performances of the present model, the results of the

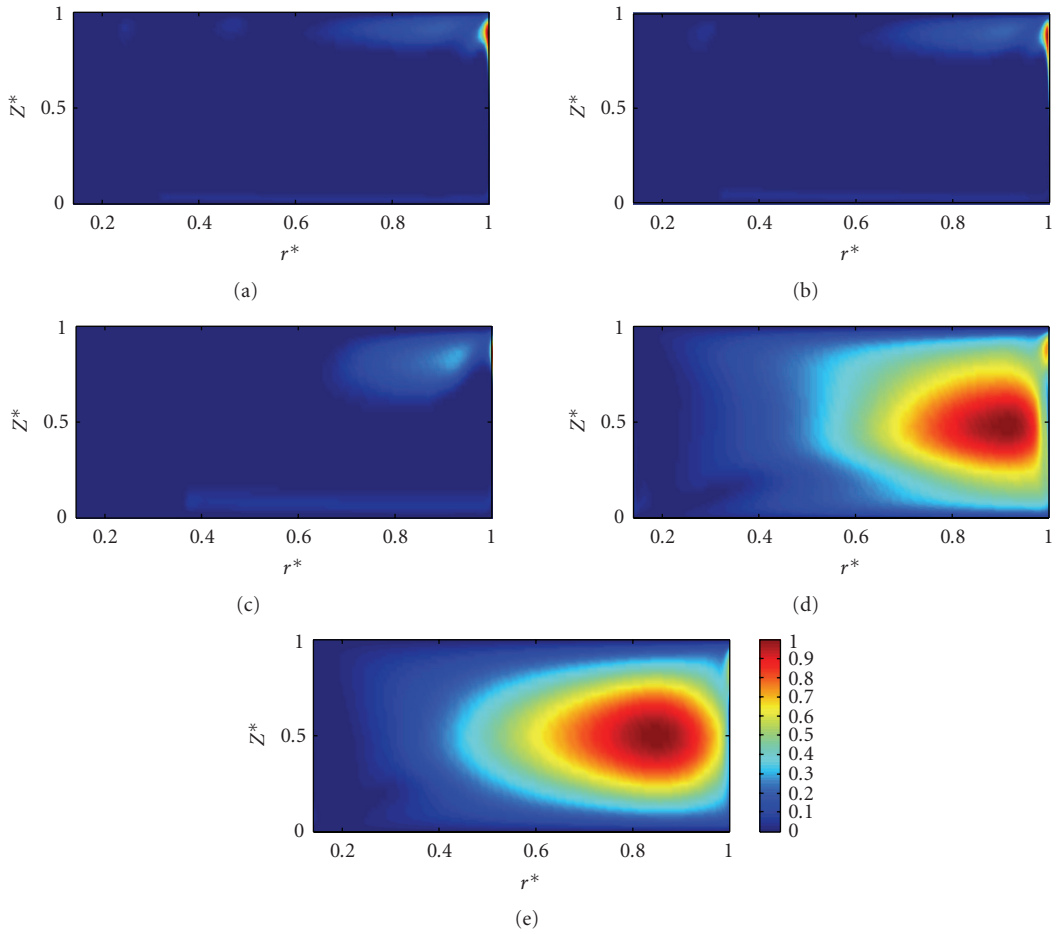

FIGURE 12: Influence of the aspect ratio on the isovalues of the turbulence Reynolds number $\mathrm{Re}_t = k^2/(\nu\varepsilon)$ (normalized by its maximum value $\mathrm{Re}_{t_{\max}}$) for various sets of flow parameters (Re, G): (a) $(1.8 \times 10^5, 0.05)$, $\mathrm{Re}_{t_{\max}} = 84.74$; (b) $(1.8 \times 10^5, 0.04)$, $\mathrm{Re}_{t_{\max}} = 78.58$; (c) $(1.8 \times 10^5, 0.02)$, $\mathrm{Re}_{t_{\max}} = 57.61$; (d) $(5 \times 10^6, 0.04)$, $\mathrm{Re}_{t_{\max}} = 2141.7$; (e) $(5 \times 10^6, 0.02)$, $\mathrm{Re}_{t_{\max}} = 2233$.

RSM code are compared to both velocity measurements performed at IRPHE by a two-component laser Doppler anemometer and numerical predictions using the k-ε model of Launder and Sharma [27] for $\mathrm{Re} = 10^6$, $G = 0.036$, and several values of the flowrate coefficient C_w.

The axial profiles of the mean radial V_r^* and tangential V_θ^* velocity components are displayed at $r^* = 0.56$ in Figures 3 and 4 for centripetal and centrifugal throughflows, respectively.

For centripetal throughflows (see Figure 3), the k-ϵ model underestimated the mean tangential velocity in the core of the flow around $z^* = 0.5$. The RSM model improves also the predictions of the mean field in the Ekman boundary layer attached to the rotating disk ($z^* \simeq 0$) and provides very satisfactory results compared to the experimental data. The main discrepancy is obtained for very large values of C_w especially along the stator side. It can be explained by considering the prerotation level of the fluid. In the RSM code, this prerotation level, which is the mean tangential velocity of the fluid in the radial gap between the rotor and the external fixed cylinder, is fixed to 0.5, whatever the value of C_w, to have a numerical code as universal as possible. In the experiments, Poncet [11] has observed that it slightly varies between 0.45 for $C_w = 0$ and 0.55 for very large values of C_w.

In the case of centrifugal superimposed throughflows (see Figure 4), the RSM model still provides better results than the k-ϵ model, which overestimates the mean tangential velocity outside the Ekman layer. The RSM model predicts quite well the transition between the Batchelor flow structure with two unmerged boundary layers (see Figure 4(b)) and the Stewartson flow structure with only one boundary layer on the rotating disk (see Figure 4(c)).

Comparisons for the three associated Reynolds stress tensor components R_{rr}^*, $R_{r\theta}^*$, and $R_{\theta\theta}^*$ are presented in Figure 5 for three characteristic values of C_w at $r^* = 0.56$. The k-ϵ model, which overestimates the turbulence intensities, does not provide good profiles. The RSM model provides very satisfactory results even close to the disks, where the highest turbulence levels are obtained. A weak discrepancy is obtained for the $R_{r\theta}^*$ component along the stator side for centripetal throughflows, which is directly linked to the underestimation of the mean radial velocity in this boundary layer.

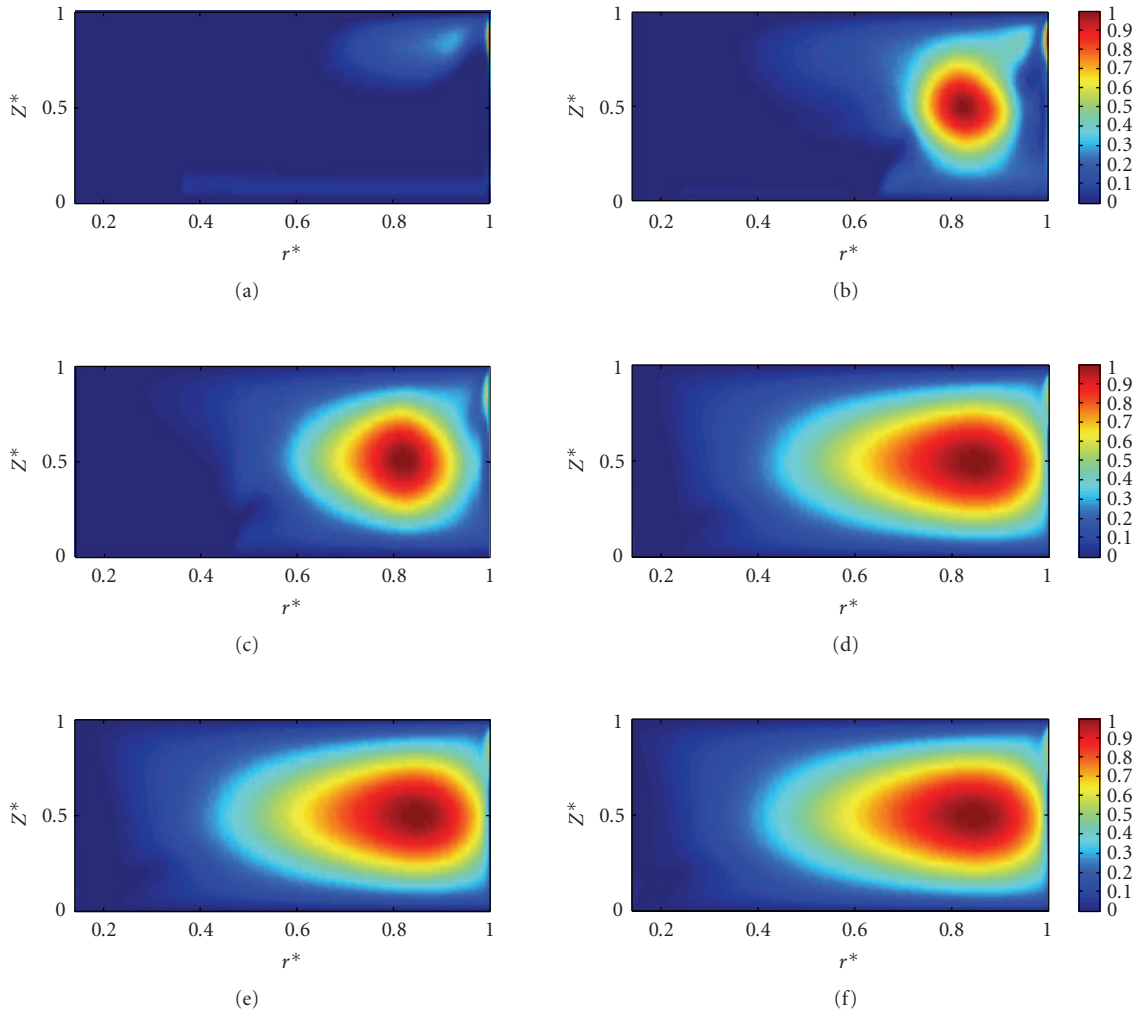

FIGURE 13: Isovalues of $\mathrm{Re}_t/\mathrm{Re}_{t_{\max}}$ for $G = 0.02$ and six values of Re: (a) 1.8×10^5, $\mathrm{Re}_{t_{\max}} = 57.61$; (b) 5×10^5, $\mathrm{Re}_{t_{\max}} = 145.13$; (c) 10^6, $\mathrm{Re}_{t_{\max}} = 464.32$; (d) 3×10^6, $\mathrm{Re}_{t_{\max}} = 1391.4$; (e) 5×10^6, $\mathrm{Re}_{t_{\max}} = 2233$; (f) 10^7, $\mathrm{Re}_{t_{\max}} = 4128.3$.

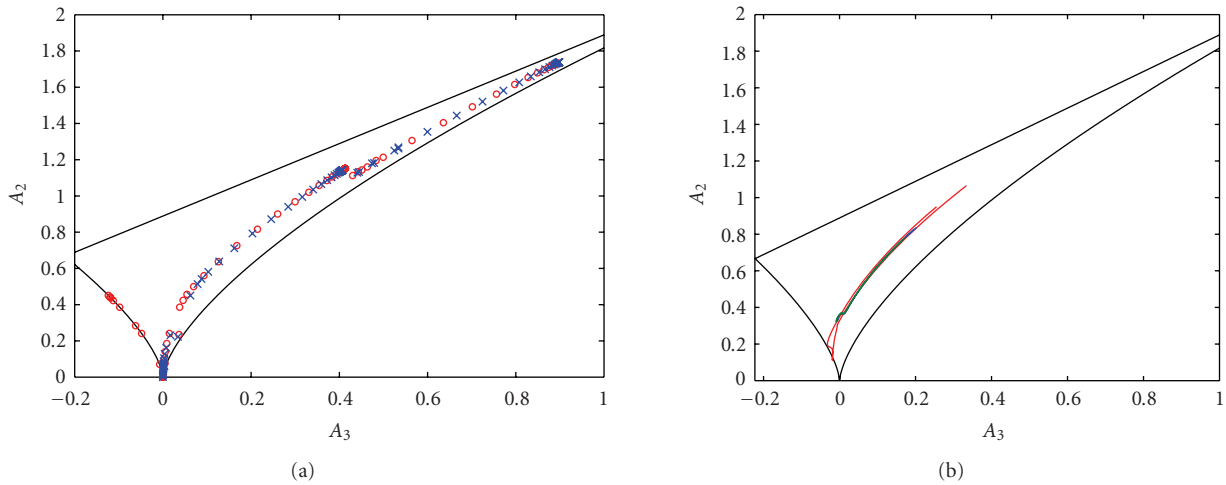

FIGURE 14: Anisotropy invariant maps at $r^* = 0.7$. (a) Influence of the aspect ratio for $\mathrm{Re} = 1.8 \times 10^5$ and $G = 0.05$ (red), $G = 0.02$ (blue); (b) influence of the Reynolds number for $G = 0.02$ and $\mathrm{Re} = 5 \times 10^5$ (red), $\mathrm{Re} = 3 \times 10^6$ (blue), and $\mathrm{Re} = 10^7$ (green).

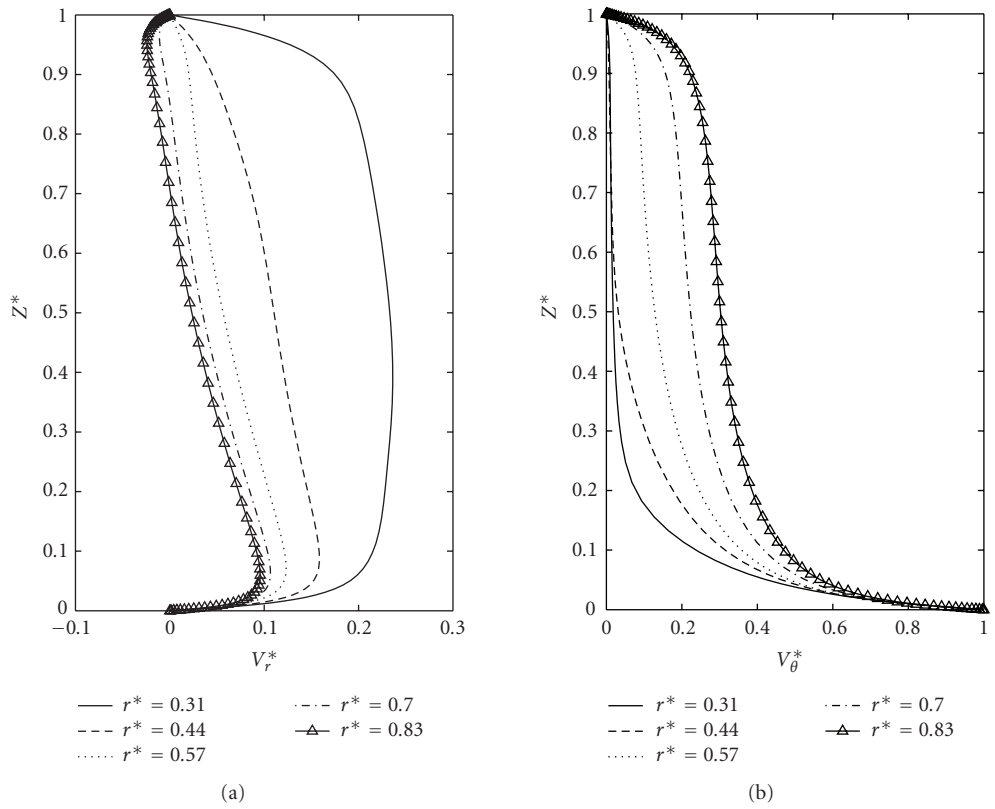

FIGURE 15: Axial profiles of the mean radial and tangential velocity components for Re = 10^6, $G = 0.02$, and $C_w = -2500$ at different radial locations r^*.

To conclude, the RSM model improves very significantly the predictions of a classical k-ε model, which is blind to any rotation effects. A very good agreement is obtained between the RSM model and LDA measurements for both the mean and turbulent fields. Some discrepancies remain along the stator in the case of very strong inward throughflows because of the different prerotation levels used in the model and measured in the experiment [11]. Considering also the previous validations in various interdisk cavities [2, 3, 25, 26], the RSM model can now be used with confidence for a parametric study of turbulent rotor-stator flows.

3. TURBULENT FLOW IN A CLOSED CAVITY

The influence on the mean and turbulent fields of both the Reynolds number Re and the aspect ratio G of the cavity is investigated in the case of an enclosed rotor-stator cavity ($C_w = 0$).

3.1. Structure of the mean flow

Figure 6 presents the axial profiles of the mean radial and tangential velocity components for Re = 10^6 and $G = 0.02$ at different radial locations in the range of $0.31 \le r^* \le 0.83$. The axial profiles of the axial mean velocity component are not shown here because $V_z^* \simeq 0$ in the whole cavity except very close to the inner and outer cylinders. According to the diagram (Re, G) of Daily and Nece [1], the flow is turbulent with merged boundary layers (regime III, see Figure 1) for these parameters. Whatever the flow parameters, rotation induces a centrifugal effect along the rotor. Thus, V_r^* remains positive. By mass conservation, V_r^* is then negative along the stator. Nevertheless, from the axial profiles, two different behaviors are obtained depending on the radial location. For $r^* = 0.31$, the flow exhibits some typical characteristics encountered in laminar rotor-stator flows with unmerged boundary layers (regime II, see Figure 1). The region of zero radial velocity and constant tangential velocity enclosed by two boundary layers developed on each disk is typical of Batchelor flows with unmerged boundary layers, whereas the local maximum of V_θ^* at the edge of the stator boundary layer as well as the very large boundary layers obtained here is typical of laminar Batchelor flows. For larger radii $r^* \ge 0.44$, the region of zero V_r^* has disappeared and V_r^* varies linearly between the disks. By increasing the values of r^*, the magnitudes of V_r^* decrease and the tangential velocity far from the disks increase. This increase is characteristic of transitional torsional Couette flows. The transition between these two behaviors observed between $r^* = 0.31$ and $r^* = 0.44$ can be explained by considering the local Reynolds number $\mathrm{Re}_r = \Omega r^2/\nu$, which is the pertinent parameter to characterize the transition between two flow regimes. Thus, $\mathrm{Re}_r = 96\,100$ for $r^* = 0.31$, whereas $\mathrm{Re}_r = 193\,600$ for $r^* = 0.44$. The value $\mathrm{Re}_r = 96\,100$ is below the critical Reynolds number for the transition between the regimes II and III [1].

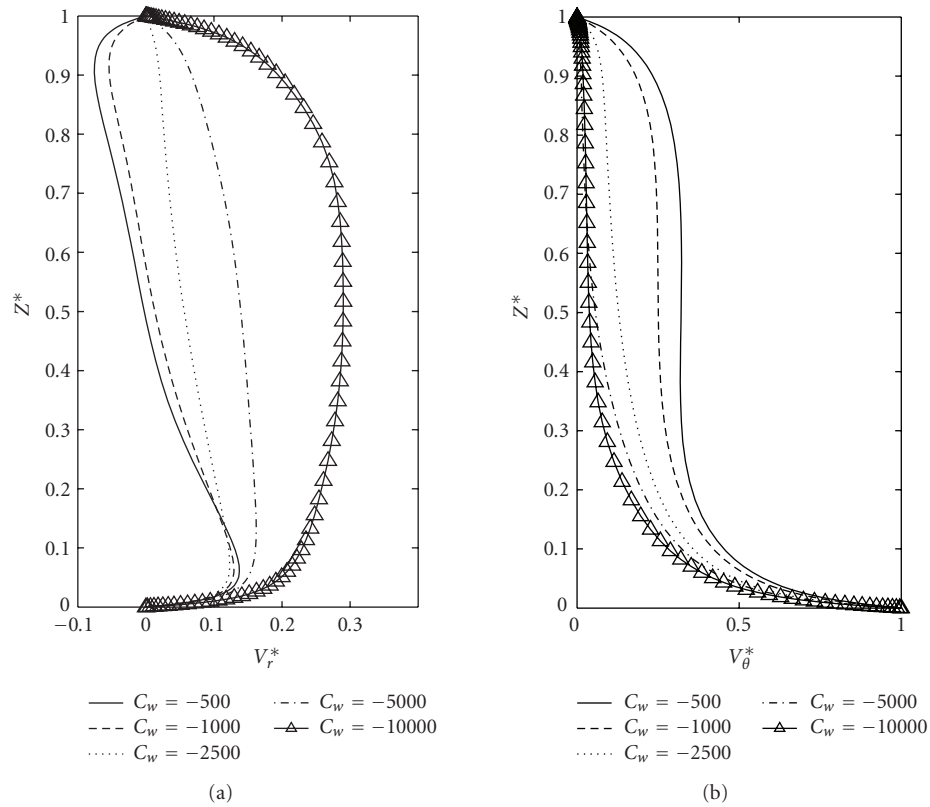

Figure 16: Axial profiles of the mean radial and tangential velocity components for $\mathrm{Re} = 10^6$, $G = 0.02$ at $r^* = 0.57$, and five flowrate coefficients $C_w < 0$.

In enclosed rotor-stator flows, the boundary layer thicknesses are an increasing function of the radial location r^* [11]. Thus, for given flow parameters, transitions between regimes II and III or between regimes II–IV and then III can occur when one moves from the rotation axis to the periphery of the cavity because of the combined increase of the boundary layer thicknesses and the turbulence levels reflected in the Re_r-values (see Cooper and Reshotko [9]).

Figure 7 presents the axial profiles of V_r^* and V_θ^* for a given aspect ratio and various Reynolds numbers in the range of $1.8 \times 10^5 \leq \mathrm{Re} \leq 10^7$ at midcavity ($r^* = 0.57$). The axial velocity V_z^* is still very weak for these parameters. The transition between the regimes I and III is here observed by varying the rotational Reynolds number. For $\mathrm{Re} = 1.8 \times 10^5$ ($\mathrm{Re}_r = 58\,482$), there is no region of zero radial velocity and the extrema of V_r^* are quite large, which is typical of regime I. For $\mathrm{Re} = 5 \times 10^5$ ($\mathrm{Re}_r = 162\,450$), the flow belongs to the regime III with a linear profile of V_r^* far from the disks and a significant decrease of the magnitudes of the V_r^* extrema. By increasing further the Reynolds number up to $\mathrm{Re} = 10^7$, the tangential velocity around midplane increases, which indicates higher turbulence levels, and the extrema of the radial velocity decrease. It agrees with the calculated results of Cooper and Reshotko [9] in the narrow gap case for Re up to 1.02×10^7.

The streamline patterns corresponding to the cases previously considered are displayed in Figures 8 and 9 to highlight the influence of the aspect ratio of the cavity and the Reynolds number, respectively. It is noteworthy that the aspect ratio of the cavity is not maintained, when one represents the streamline patterns to enable a better visualization of the flow structure. Streamlines parallel to the rotation axis around midcavity ($z^* \simeq 0.5$) as in Figure 8(a) are typical of a Batchelor-like flow. For $\mathrm{Re} = 1.8 \times 10^5$, it is the case for the largest aspect ratios $G = 0.05$ (see Figure 8(a)) and 0.04 (see Figure 8(b)). For the lower value $G = 0.02$ (see Figure 8(c)), the streamline patterns get curved and are characteristic of torsional Couette flows. When one increases the Reynolds number up to 5×10^6, the flow structure is not so clear. Close to the rotation axis, streamlines are parallel to the axis (the boundary layers are unmerged) and get inclined at the periphery (the boundary layers are merged) both for $G = 0.04$ (see Figure 8(d)) and 0.02 (see Figure 8(e)). Whatever the flow parameters, a recirculation bubble appears along the external cylinder around midplane.

For a given aspect ratio $G = 0.02$, Figure 9 highlights the effect of the rotation rate reflected in the values of the Reynolds number Re on the streamline patterns. For $\mathrm{Re} = 1.8 \times 10^5$ (see Figure 9(a)), the flow exhibits a torsional Couette flow behavior. By increasing the values of Re (see Figures 9(b)–9(f)), the streamlines get aligned with

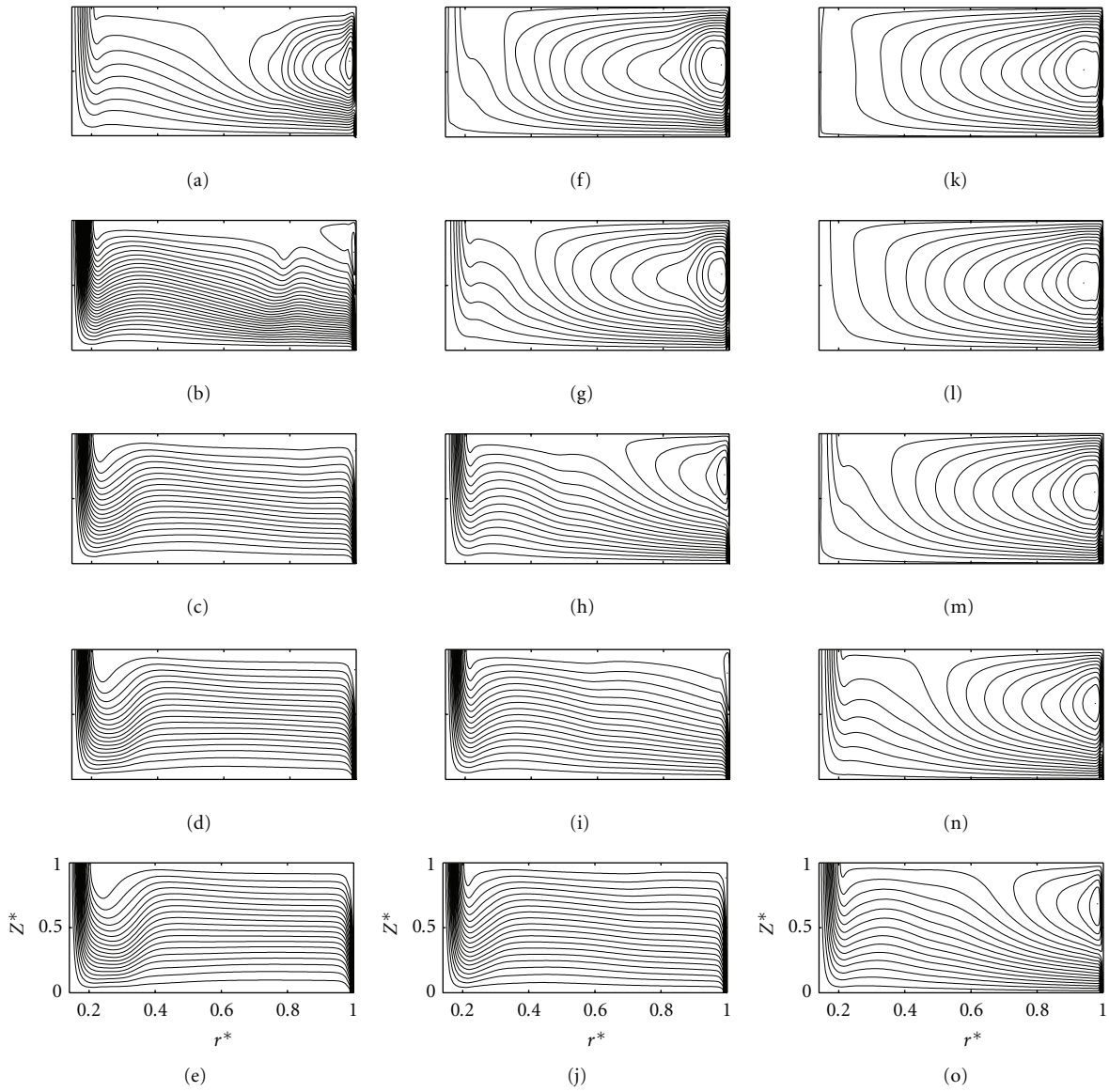

Figure 17: 20 streamline patterns Ψ^* for $G = 0.02$ and various sets of parameters (Re, C_w): (a) $(1.8 \times 10^5, -500)$, $-3.67 \le \Psi^* \le 125.06$; (b) $(1.8 \times 10^5, -1000)$, $-1.56 \le \Psi^* \le 118.96$; (c) $(1.8 \times 10^5, -2500)$, $-2.32 \le \Psi^* \le 278.67$; (d) $(1.8 \times 10^5, -5000)$, $-4.65 \le \Psi^* \le 557.79$; (e) $(1.8 \times 10^5, -10\,000)$, $-9.29 \le \Psi^* \le 1116.8$; (f) $(10^6, -500)$, $-12.52 \le \Psi^* \le 52.55$; (g) $(10^6, -1000)$, $-7.7 \le \Psi^* \le 56.67$; (h) $(10^6, -2500)$, $-0.79 \le \Psi^* \le 67.75$; (i) $(10^6, -5000)$, $-0.84 \le \Psi^* \le 105.93$; (j) $(10^6, -10\,000)$, $-1.67 \le \Psi^* \le 201.81$; (k) $(5 \times 10^6, -500)$, $-19.49 \le \Psi^* \le 36.54$; (l) $(5 \times 10^6, -1000)$, $-17.52 \le \Psi^* \le 37.56$; (m) $(5 \times 10^6, -2500)$, $-13.14 \le \Psi^* \le 41.05$; (n) $(5 \times 10^6, -5000)$, $-7.39 \le \Psi^* \le 46.44$; (o) $(5 \times 10^6, -10\,000)$, $-1.06 \le \Psi^* \le 56.02$.

the z direction close to the axis, which characterizes a flow with unmerged boundary layers. In the same time, the flow remains with merged boundary layers at largest radii. A small recirculation bubble due to confinement is still observed along the shroud. One noticeable effect is also the curvature of the streamlines close to the disks and for small r^*. A strong curvature of the streamlines close to the walls indicate strong extrema of the radial velocity V_r^* in the boundary layers, which is typical of laminar rotor-stator flows, whereas a weak curvature is associated with turbulent flows. This change is quite visible by comparing the flow structures close to the axis between Figures 9(c) and 9(e), for example.

3.2. Turbulence statistics

The influence of the different parameters on the turbulent field is now investigated. Figure 10 shows the axial profiles of the six components of the Reynolds stress tensor at given Reynolds number $\mathrm{Re} = 10^6$ and aspect ratio $G = 0.02$ for various radii in the range of $0.31 \le r^* \le 0.83$ corresponding to the mean velocity profiles presented in Figure 6. Close to the rotation axis at $r^* = 0.31$, turbulence is mainly concentrated in the boundary layers (as the boundary layers are unmerged at this radius), whereas the core of the flow is laminar. When one moves toward the periphery, the

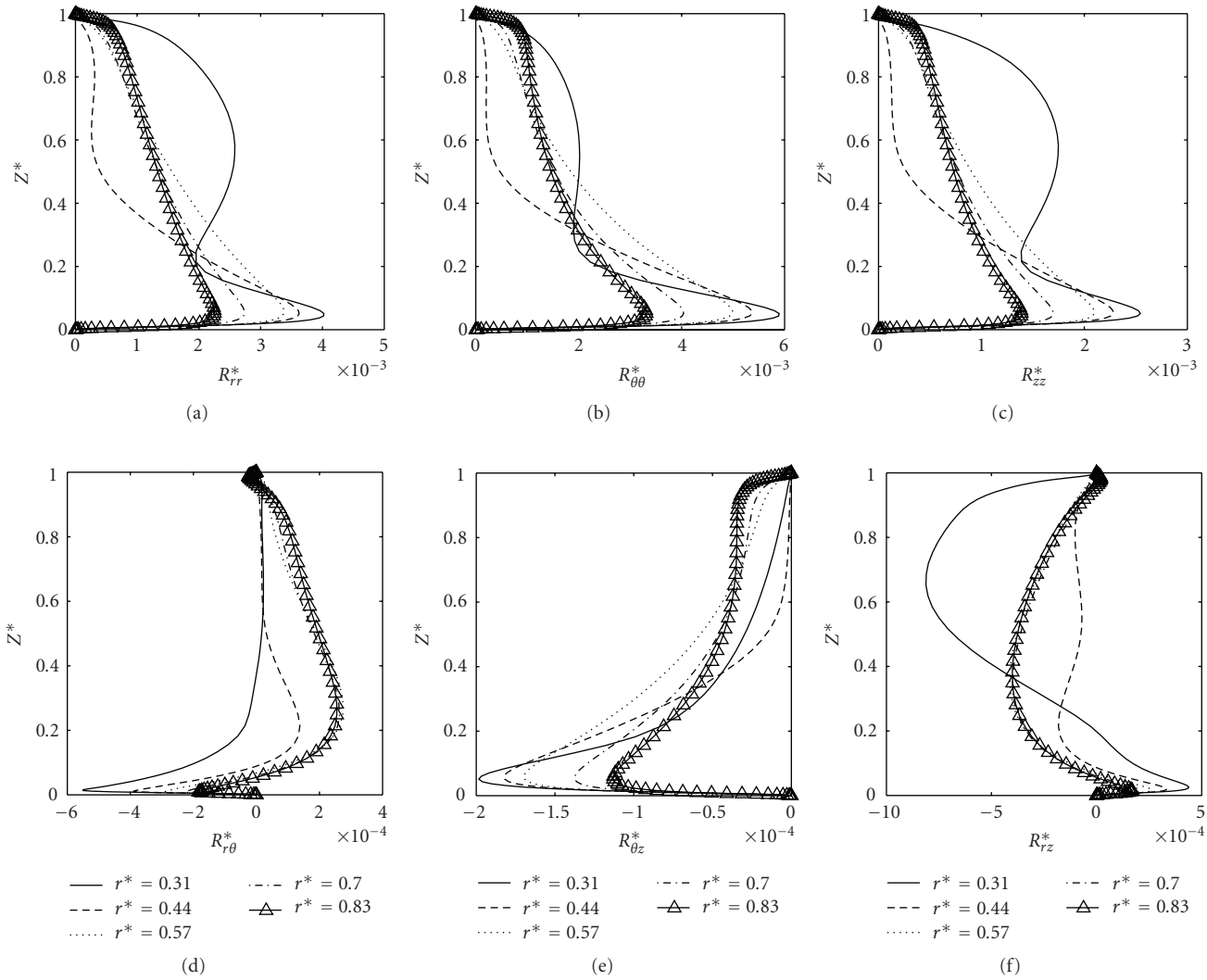

FIGURE 18: Axial profiles of the six Reynolds stress tensor components for Re $= 10^6$, $G = 0.02$, and $C_w = -2500$ at different radial locations r^*.

turbulence intensities increase because of the increase of the local Reynolds number Re_r, which is proportional to the local radius to power 2. The maximum of the normal stresses, located close to the rotor, is reached at $r^* = 0.57$ and remains the same for larger radii. On the other hand, there is a significant increase of the normal stresses both along the stationary disk and around midplane, when one increases r^*. Finally, at the periphery of the cavity, turbulence intensities are almost constant along the axial direction apart very close to the disks, where they vanish. Finally, contrary to turbulent Batchelor flows (regime IV [1]) where turbulence is concentrated in the boundary layers, whereas the core of the flow is laminar [3, 11], turbulence in torsional Couette flows (regime III [1]) is distributed along the axial direction. Moreover, the levels of the normal stresses are quite comparable (the order of 10^{-3}), which is not the case for Batchelor flows, where R^*_{zz} is generally negligible compared to the other normal components [3, 11]. The cross-components of the Reynolds stress tensor are also not so weak here as in Batchelor flows. Their levels increase when moving toward the periphery.

The influence of the Reynolds number on the six Reynolds stress tensor components is assessed in Figure 11 at $r^* = 0.57$ and for $G = 0.02$. As expected, when Re is increased, higher turbulence intensities are obtained. For Re $= 1.8 \times 10^5$, turbulence is confined along the rotor, whereas the flow remains laminar everywhere else. For Re $= 5 \times 10^5$, the flow along the stationary disk gets turbulent. It is a noticeable difference with turbulent Batchelor flows. When the aspect ratio is sufficiently large to ensure unmerged boundary layers, the Bödewadt layer attached to the stator is more unstable than the Ekman layer attached to the rotor [3, 11] and gets turbulent for smaller values of the local Reynolds number. On the contrary, for torsional Couette flows (at midcavity, $r^* = 0.57$), the flow along the rotating disk is found to be more turbulent than along the stator. For Re $\geq 5 \times 10^6$, there is no significant effect of the Reynolds number on the turbulence intensities.

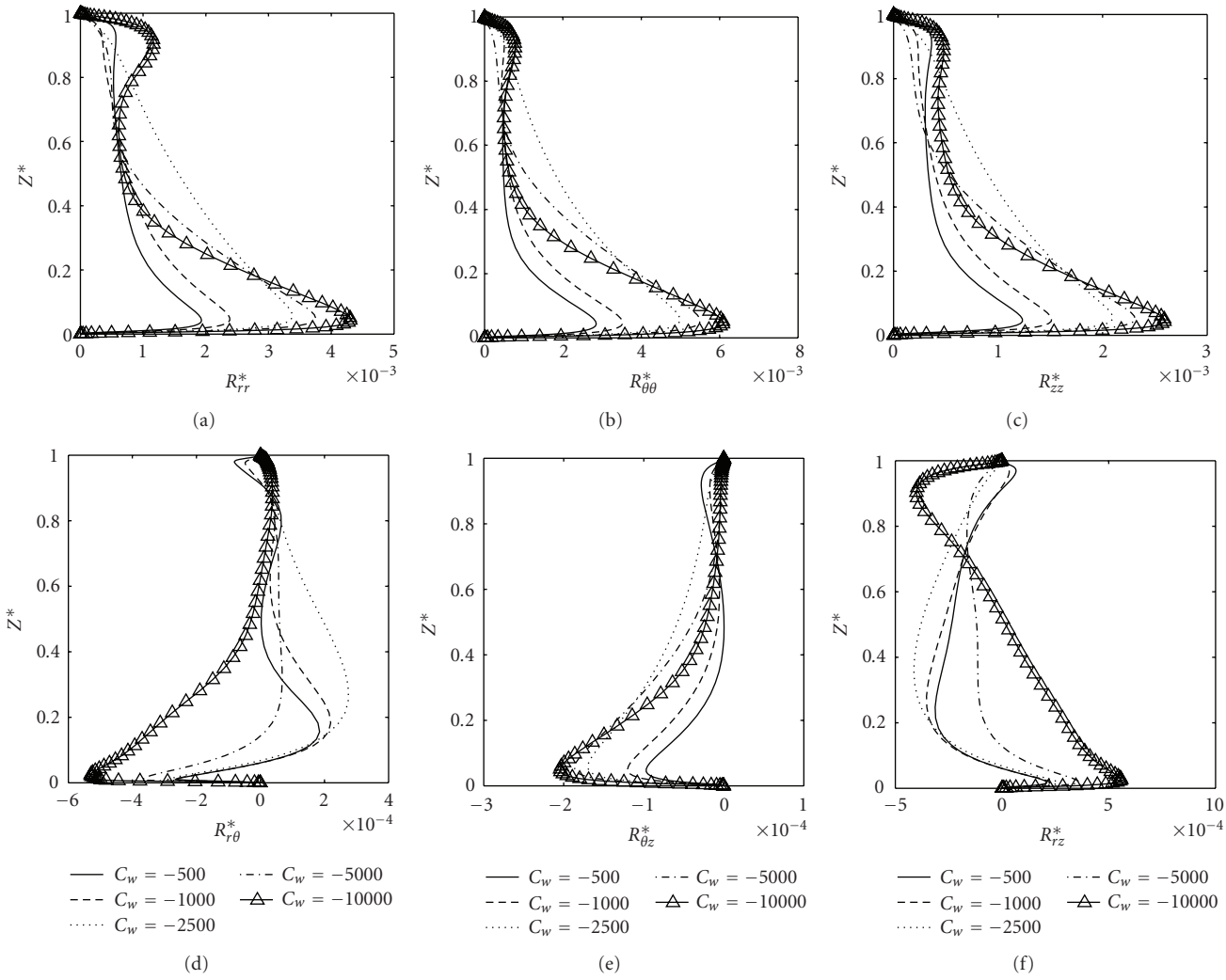

FIGURE 19: Axial profiles of the six Reynolds stress tensor components for $\mathrm{Re} = 10^6$, $G = 0.02$ at $r^* = 0.57$ and five flowrate coefficients $C_w < 0$.

The isovalues of the turbulence Reynolds number $\mathrm{Re}_t = k^2/(\nu\varepsilon)$ enable us to visualize the turbulent regions of the flow. The flow is considered as being laminar for $\mathrm{Re}_t \leq 1/c_\mu \simeq 11$ ($c_\mu = \nu_t\epsilon/k^2 = 0.09$, where ν_t is the turbulence viscosity). Figure 12 presents some maps of Re_t in a (r, z) plane for various flow conditions (Re, G). Whatever the flow parameters, the maximum of Re_t, denoted by $\mathrm{Re}_{t_{\max}}$, is localized at the periphery of the cavity, where the highest values of the local Reynolds number are obtained. For a moderate Reynolds number $\mathrm{Re} = 1.8 \times 10^5$ and $G \geq 0.02$ (see Figures 12(a)–12(c)), the maximum of Re_t is localized at the junction between the shroud and the stator along the Stewartson layer attached to the external cylinder. $\mathrm{Re}_{t_{\max}}$ decreases with decreasing the values of the aspect ratio. If the Reynolds number is increased up to $\mathrm{Re} = 5\times10^6$ (see Figures 12(d)-12(e)), $\mathrm{Re}_{t_{\max}}$ is 27 (resp., 39) times larger for $G = 0.04$ (resp., $G = 0.02$). The flow is then turbulent in the whole cavity with higher turbulence levels at largest radii.

Figure 13 presents the influence of the rotational Reynolds number, in the range of $1.8 \times 10^5 \leq \mathrm{Re} \leq 10^7$, on the maps of the turbulence Reynolds number Re_t for a given aspect ratio $G = 0.02$ corresponding to torsional Couette flows with merged boundary layers. As expected, $\mathrm{Re}_{t_{\max}}$ increases with increasing values of Re: from $\mathrm{Re}_{t_{\max}} = 57.61$ for $\mathrm{Re} = 1.8\times10^5$ to $\mathrm{Re}_{t_{\max}} = 4128.3$ for $\mathrm{Re}= 10^7$. $\mathrm{Re}_{t_{\max}}$ remains localized close to the shroud but the radial extent of the turbulent regions increases with Re too.

Figure 14 shows the anisotropy invariant map for the Reynolds stress tensor at $r^* = 0.7$ for various sets of parameters (Re, G). The second A_2 and third A_3 invariants of the anisotropy tensor a_{ij} of the second moments of the fluctuations are defined as $A_2 = a_{ij}a_{ji}$ and $A_3 = a_{ij}a_{jk}a_{ki}$ [28]. The results of the RSM model respect the realizability diagram of Lumley [28] as they remain within the region delimited by the two lines corresponding to the axisymmetric flow $A_3 = \pm A_2^{3/2}/\sqrt{6}$ and the straight upper one corresponding to the two-component limit $A_3 = A_2 - 8/9$. The influence of the aspect ratio on the anisotropy invariant map is large for $\mathrm{Re} = 1.8 \times 10^5$ (see Figure 14(a)). For $G = 0.05$, the flow exhibits a Batchelor-like structure

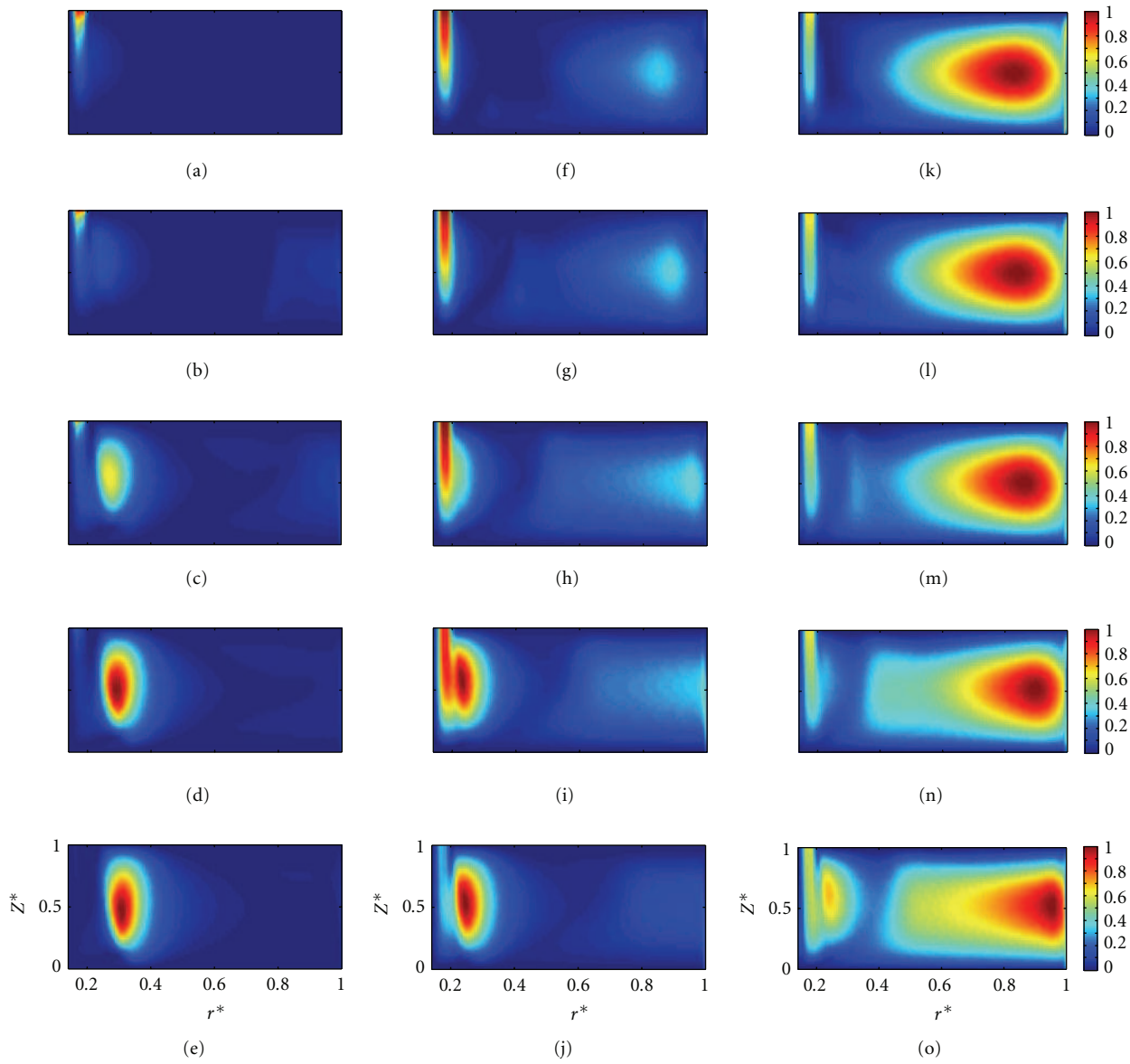

FIGURE 20: Isovalues of $\mathrm{Re}_t/\mathrm{Re}_{t_{\max}}$ for $G = 0.02$ and various sets of parameters (Re, C_w): (a) $(1.8\times10^5, -500)$, $\mathrm{Re}_{t_{\max}} = 1497.7$; (b) $(1.8\times10^5, -1000)$, $\mathrm{Re}_{t_{\max}} = 1483.4$; (c) $(1.8\times10^5, -2500)$, $\mathrm{Re}_{t_{\max}} = 1293.5$; (d) $(1.8\times10^5, -5000)$, $\mathrm{Re}_{t_{\max}} = 2019.1$; (e) $(1.8\times10^5, -10\,000)$, $\mathrm{Re}_{t_{\max}} = 4535.6$; (f) $(10^6, -500)$, $\mathrm{Re}_{t_{\max}} = 1499.8$; (g) $(10^6, -1000)$, $\mathrm{Re}_{t_{\max}} = 1499.9$; (h) $(10^6, -2500)$, $\mathrm{Re}_{t_{\max}} = 1499.2$; (i) $(10^6, -5000)$, $\mathrm{Re}_{t_{\max}} = 1752.4$; (j) $(10^6, -10\,000)$, $\mathrm{Re}_{t_{\max}} = 4410.7$; (k) $(5\times10^6, -500)$, $\mathrm{Re}_{t_{\max}} = 2169.4$; (l) $(5\times10^6, -1000)$, $\mathrm{Re}_{t_{\max}} = 2199.6$; (m) $(5\times10^6, -2500)$, $\mathrm{Re}_{t_{\max}} = 2282.8$; (n) $(5\times10^6, -5000)$, $\mathrm{Re}_{t_{\max}} = 2420.5$; (o) $(5\times10^6, -10\,000)$, $\mathrm{Re}_{t_{\max}} = 2642.1$.

(see Figure 8(a)) and for $0.22 \le z^* \le 0.45$, the invariant map follows the axisymmetric curve ($A_3 < 0$), which is not the case for the other value of G corresponding to a torsional Couette flow structure (see Figure 8(c)). For $G = 0.05$ and $G = 0.02$, turbulence tends to the one-component limit (large values of A_2 and A_3) close to the disks. The influence of the Reynolds number on the invariant anisotropy map of torsional Couette flows ($G = 0.02$) remains weak (see Figure 14(b)). The map for $\mathrm{Re} = 1.8\times10^5$ has already been discussed. In this case, the flow is laminar at this radial location (see Figure 13(a)). If Re is increased to values larger than 5×10^5, the flow gets turbulent at this radius (Figures 13(b)–13(f)) and the anisotropy invariant map is then changed. Turbulence follows mainly a three-component behavior and the one-component tendency close to the disks has disappeared. The same maps are obtained for radial locations in the range of $0.3 \le r^* \le 0.9$. Close to the cylinders, the curves tend to the two-component limit as the wall normal fluctuations are damped more effectively than fluctuations parallel with the cylinders. Thus, the flatness parameter A is equal to 0. Note that Poncet [11] showed that the structural anisotropy is axisymmetric whatever the flow conditions, which is due to the choice of the dimensionality tensor in the RSM model. Thus, turbulence is two dimensional with cigar-shaped vortex aligned with the rotation axis.

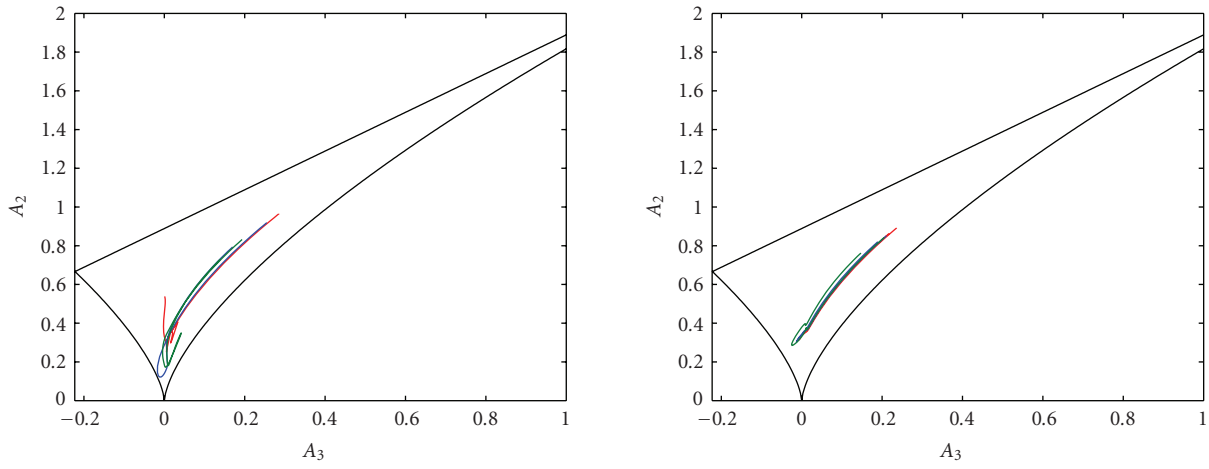

FIGURE 21: Anisotropy invariant map at (a) $r^* = 0.3$ and (b) $r^* = 0.7$ for $\mathrm{Re} = 10^6$, $G = 0.02$ and three flowrate coefficients: $C_w = -500$ (red), $C_w = -2500$ (blue), and $C_w = -10\,000$ (green).

4. TURBULENT FLOW WITH AN AXIAL THROUGHFLOW

In the following, the value of the aspect ratio is fixed to $G = 0.02$ and the influence of an axial flow is investigated on the mean and turbulent fields for various radial locations, Reynolds numbers, and flowrate coefficients.

4.1. *Case of a centrifugal throughflow*

In this subsection, an axial centrifugal throughflow, characterized by a negative flowrate coefficient $C_w < 0$, is superimposed on the mean tangential flow due to rotation.

4.1.1. *Structure of the mean flow*

Figure 15 displays the velocity profiles corresponding to the case $\mathrm{Re} = 10^6$ and $C_w = -2500$ at five radial positions and Figure 17(h) brings out the corresponding streamlines. Depending on the radial location, the flow belongs to the torsional Couette or Stewartson type of flow. For $r^* = 0.31$, the flow exhibits a Stewartson-like structure from the V_θ^*-profiles with only one boundary layer on the rotor. The corresponding radial velocity which is always positive becomes significant compared to the tangential velocity: the flow is then fully centrifugal and the mean radial velocity profile gets closer to a Poiseuille-like profile at this radius. Phadke and Owen [8] found that the flowrate coefficient necessary to obtain the transition between torsional Couette and Stewartson flow structures can be scaled as $|C_w| = 0.219\mathrm{Re}^{4/5} r^{*13/5}$. Thus, for the set of parameters considered in Figure 15, the transition should occur for $r^* = 0.51$. The transition between these two behaviors is continuous and appears here for $r^* = 0.48$, which is in excellent agreement with the empirical value given by Phadke and Owen [8]. The small discrepancy may be attributed to the different geometries considered. In their case, there is no hub attached to the rotor and the throughflow is pulling out radially at the outlet of the cavity.

When moving toward the periphery of the cavity, the flow switches progressively to torsional Couette type with $V_\theta^* \to 0.4$ for increasing values of r^*, while the flow along the stator gets centripetal. Moreover, the axial profile of V_r^* around midplane gets linear, which indicates a strong shear around midplane. At intermediate radial locations, V_r^* is larger along the rotor, which is due to the combine effect of the centrifugal superimposed throughflow and the centrifugal effect due to the rotating disk. For this set of parameters, a large recirculation is observed at the corner between the shroud and the stator (see Figure 17(h)).

As it can be seen from the axial profiles of the mean velocity profiles (see Figure 16) but also from the streamline patterns (see Figures 17(f)–17(j)), the flow structure switches from torsional Couette type for small values of $|C_w| \leq 10^3$ to Stewartson type for larger values $|C_w| \geq 5 \times 10^3$ at $\mathrm{Re} = 10^6$ and $r^* = 0.57$. The transition appears for $2500 \leq |C_w| \leq 5000$, in accordance with the empirical law of Phadke and Owen [8], which gives $|C_w| = 3204$ for the transition. When the flow exhibits a Stewartson flow structure, the flow is mainly dominated by the superimposed throughflow, whose effect is dominant compared to the one of rotation. For a torsional Couette flow structure, rotation has a preponderant effect compared to the axial throughflow. Note that whatever the set of parameters (G, Re, $C_w < 0$, r^*) is, the mean axial velocity component remains very weak apart along the hub and the shroud.

The streamlines are displayed in Figure 17 for a given aspect ratio $G = 0.02$ and 15 flow conditions: three values of the Reynolds number $\mathrm{Re} = 1.8 \times 10^5$ (see Figures 17(a)–17(e)), 10^6 (see Figures 17(f)–17(j)), and 5×10^6 (Figures 17(k)–17(o)) and five flowrate coefficients $C_w = -500, -10^3, -2.5 \times 10^3, -5 \times 10^3$, and -10^4.

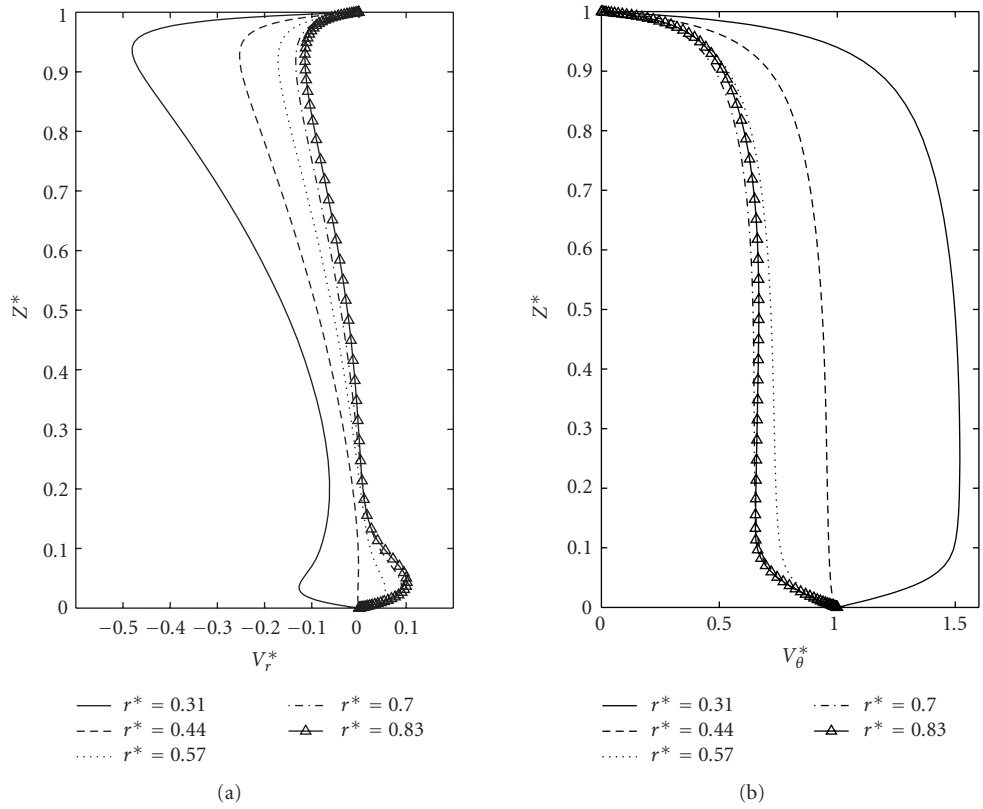

Figure 22: Axial profiles of the mean radial and tangential velocity components for Re = 10^6, $G = 0.02$, and $C_w = 2500$ at different radial locations r^*.

(i) For Re = 1.8×10^5, rotation has a dominant effect on the flow structure at the lowest value of $C_w = -500$ at the periphery of the cavity where the recirculation zone is obtained (see Figure 17(a)). Closer to the rotation axis, the flow is dominated by the outward throughflow since the streamlines are parallel to the disks. For $C_w = -10^3$, the recirculation zone is smaller (see Figure 17(b)) and disappears completely for higher flowrates $|C_w| \geq 2500$ (see Figures 17(c)–17(e)). The flow is then purely centrifugal with streamlines parallel to the disks.

(ii) For Re = 10^6, apart in the region very close to the rotation axis when the centrifugal throughflow enters the cavity, the flow is mainly dominated by rotation for $C_w = -500$ (see Figure 17(f)). For $C_w = -10^3$, the flow is purely centrifugal for $r^* \leq 0.4$ and gets torsional Couette type in the outer part of the cavity (see Figure 17(g)). When one increases further the magnitude of the throughflow up to $|C_w| = 2500$ (see Figure 17(h)), the recirculation bubble gets smaller and disappears for $|C_w| \geq 5000$ (see Figures 17(i)-17(j)).

(iii) For Re = 5×10^6, the same scenario is obtained when one increases the values of $|C_w|$. The flow exhibits a torsional Couette flow structure for $C_w = -500$ (see Figure 17(k)) and $C_w = -10^3$ (see Figure 17(l)). The size of the recirculation bubble decreases for increasing the values of $|C_w|$ up to 10^4 but it does not disappear for this high Reynolds number. Rotation has still a dominant effect at the periphery of the cavity, where high values of the local Reynolds number prevail.

4.1.2. Turbulence statistics

Figure 18 exhibits the axial profiles of the six Reynolds stresses for Re = 10^6, $G = 0.02$, and $C_w = -2500$ at five radial locations. As for turbulent Batchelor flows (regime IV) with inward throughflow [3], turbulence intensities are higher along the rotating disk and vanish toward the stationary disk. Contrary to the case of a closed cavity $C_w = 0$, they decrease when moving toward the periphery of the cavity, whereas the local Reynolds number is increased. Turbulence is then mainly controlled by the imposed throughflow, whose influence on turbulence is preponderant compared to rotation. It is confirmed by the maps (see Figure 20) of the isoturbulence Reynolds number Re_t (detailed below), which show that turbulence is confined at the inlet of the throughflow close to the rotation axis.

At a given radial location $r^* = 0.57$, Figure 19 shows the influence of the flowrate coefficient on the Reynolds stresses. Turbulence intensities increase for increasing values of $|C_w|$ but the effect of the throughflow gets weaker for $|C_w| \geq 5000$. The magnitudes of the normal components of the Reynolds stress tensor are quite comparable for this range of parameters. They all vanish at the stator surface. In

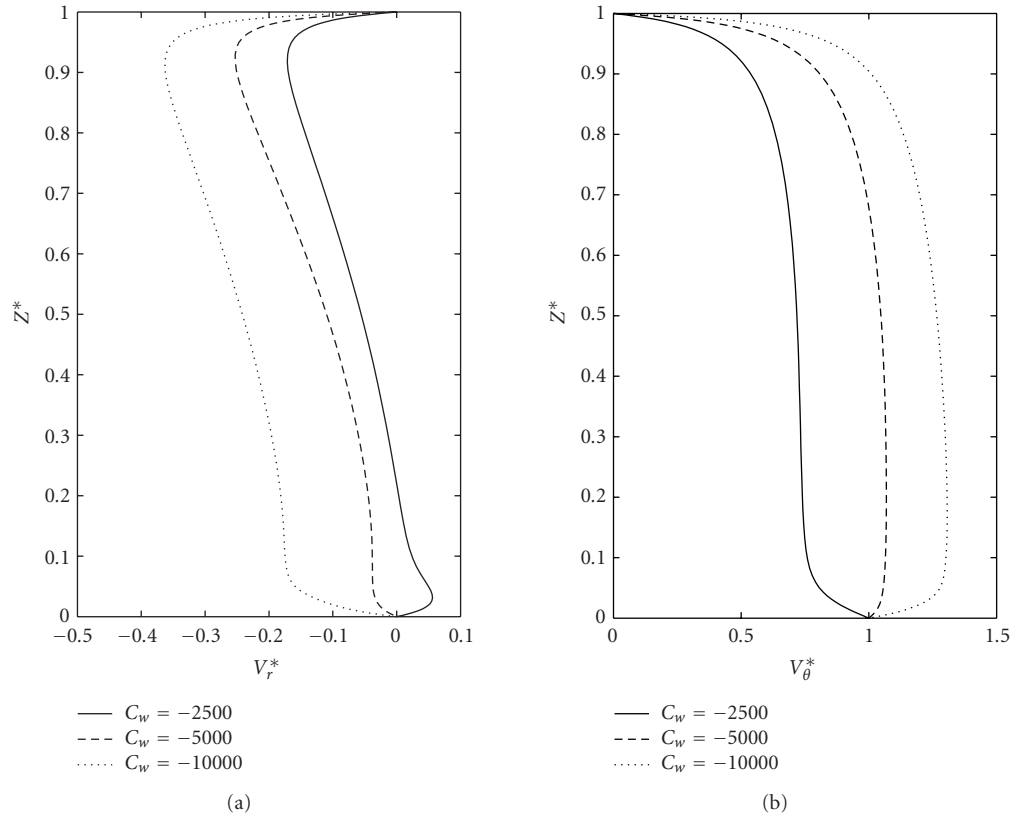

FIGURE 23: Axial profiles of the mean radial and tangential velocity components for Re = 10^6, $G = 0.02$ at $r^* = 0.57$ and three flowrate coefficients $C_w > 0$.

the same way, the cross-components of the Reynolds stress tensor are maximum along the rotating disk, which indicates a very strong shear stress induced by a combined effect of the throughflow and the rotation and vanish toward the stationary disk.

Compared to the case without throughflow $C_w = 0$, when an outward throughflow is superimposed on the mean tangential flow, the maps of the turbulence Reynolds number Re_t are clearly modified (see Figure 20). Whatever the Reynolds number is, the maximum of Re_t is an increasing function of the magnitude of the flowrate coefficient C_w, especially for $|C_w| \geq 5000$. For Re = 1.8×10^5 and 10^6, the flow is mainly dominated by the imposed throughflow. Thus, $\mathrm{Re}_{t_{\max}}$ is located along the hub in the inlet region. This maximum is slightly shifted to larger radii, when $|C_w|$ is increased. For the highest Reynolds number Re = 5×10^6 (see Figures 20(k)–20(o)), turbulence is produced by a combined effect of the high rotation rate and the strong incoming jet. The highly turbulent flow regions are then located both at the inlet and at the periphery of the cavity. The iso-Re_t patterns resemble the ones obtained in a closed cavity (see Figure 13(e)).

As shown in Figure 21(b), the anisotropy invariant maps are not modified by an imposed outward throughflow compared to the closed cavity case (see Figure 14(b)) for $r^* = 0.7$ and turbulent torsional Couette flows (Re = 10^6, $G = 0.02$). Turbulence is mainly composed of three components, whatever the values of the flowrate coefficient C_w. It is not the case closer to the rotation axis at $r^* = 0.3$ (see Figure 21(a)), where the curves tend to the isotropic case ($A_3 = A_2 = 0$) for centrifugal flows, whereas we recall that turbulence tends to the one-component limit in a closed cavity. In the isotropic case, the flatness parameter A is equal to 1.

4.2. Case of a centripetal throughflow

An axial outward throughflow, characterized by a positive flowrate coefficient $C_w > 0$, is now superimposed on the mean tangential flow. The inlet of the jet is then located at the periphery of the cavity and the outlet is confined between the hub and the stator.

4.2.1. Structure of the mean flow

Figure 22 represents the axial profiles of the dimensionless tangential and radial velocity components for Re = 10^6, $G = 0.02$, and $C_w = 2500$. We first analyze the influence of the radial position in the range of $0.31 \leq r^* \leq 0.83$. The corresponding streamlines are displayed in Figure 24(d). In the outer half of the cavity $r^* \geq 0.57$, where a large recirculation is observed, the flow structure is quite similar

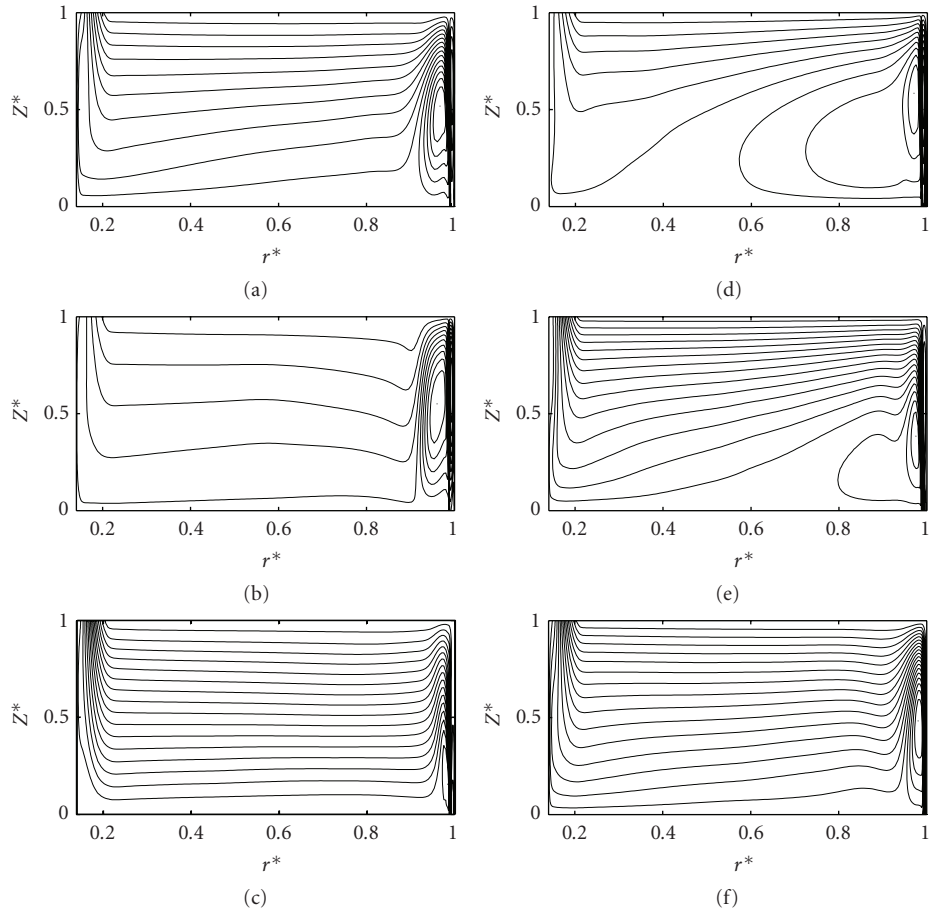

Figure 24: 20 streamline patterns Ψ^* for $G = 0.02$ and six sets of parameters (Re, C_w): (a) $(1.8 \times 10^5, 2500)$, $-398.68 \leq \Psi^* \leq 151.17$; (b) $(1.8 \times 10^5, 5000)$, $-714.6 \leq \Psi^* \leq 115.9$; (c) $(1.8 \times 10^5, 10\,000)$, $-1274.1 \leq \Psi^* \leq 82.89$; (d) $(10^6, 2500)$, $-127.01 \leq \Psi^* \leq 37.5$; (e) $(10^6, 5000)$, $-117.11 \leq \Psi^* \leq 23.18$; (f) $(10^6, 10\,000)$, $-201.77 \leq \Psi^* \leq 58.8$.

to the one obtained in a closed cavity $C_w = 0$: the fluid is centrifugal due to rotation along the rotor and is centripetal along the stator by conservation of mass. Between these two flow regions, the axial profile of the radial velocity is almost linear and the tangential velocity is almost constant and still inferior to the local disk velocity ($V_\theta^* < 1$). For $r^* = 0.44$, the fluid in the main part of the interdisk spacing rotates at the same angular velocity than the rotating disk. The radial velocity along this disk is then equal to zero. When one approaches further the rotation axis, at $r^* = 0.31$, V_θ^* increases and the fluid rotates 50% faster than the rotor. Indeed, because of the conservation of the angular momentum, a fluid particle increases its rotation when flowing to the center. V_r^* is then negative whatever the axial position and the flow is purely centripetal. This behavior has been observed also for turbulent Batchelor flows by Poncet et al. [3].

When the local radius is fixed to $r^* = 0.57$ and we vary the flowrate coefficient C_w from 2500 to 10^4, the same phenomenon is obtained (see Figure 23). For low values of C_w, the velocity profiles are quite similar to the case $C_w = 0$. For $C_w = 5000$, the fluid rotates at the same angular velocity as the rotor and the radial velocity is then equal to zero along the rotating disk. By increasing further C_w up to 10^4, by conservation of the angular momentum, V_θ^* gets larger than 1 and the flow is purely centripetal. As in the case of a centrifugal throughflow, the mean axial velocity component remains very weak apart along the hub and the shroud when an inward throughflow is superimposed.

Regarding the corresponding streamline patterns (see Figure 24), it appears that the inward throughflow has a dominant effect on the flow structure compared to the effect of rotation. At the inlet, when the axial jet impinges the stator, one part of the fluid is moving inwards toward the axis of rotation along the stator and the other part is centrifugal due to the rotation of the disk. Thus, a large recirculation is created at the periphery of the cavity (see Figure 24(d)). In that case, the flow exhibits the same structure as in a closed cavity for large radii and the fluid rotates faster than the disk close to the axis. For a given Reynolds number $\mathrm{Re} = 10^6$, when the flowrate is increased to 10^4 (see Figure 24(f)), the flow is dominated by the incoming axial jet. The flow is purely centripetal and the streamlines are then parallel to the disks as in the centrifugal case.

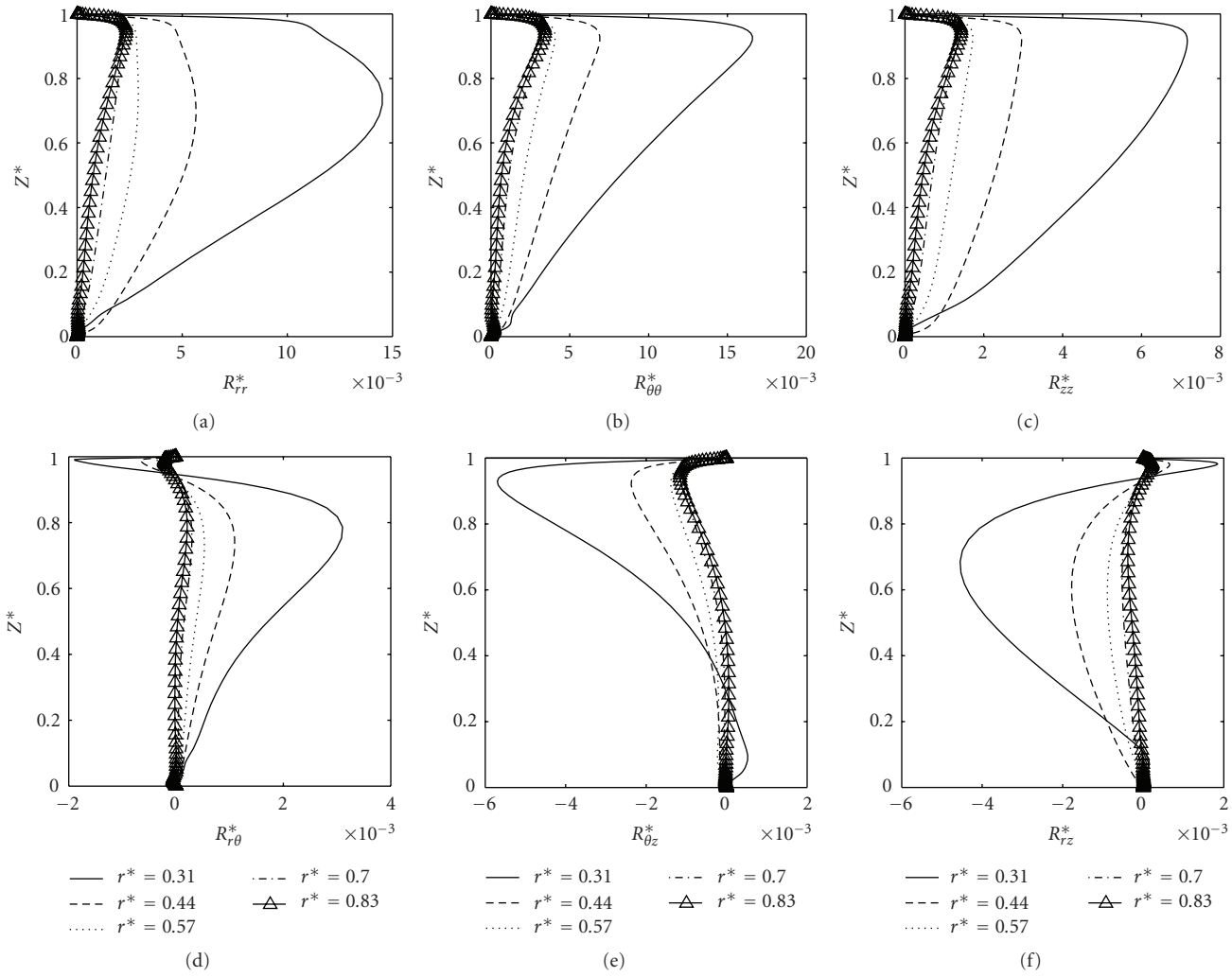

FIGURE 25: Axial profiles of the six Reynolds stress tensor components for Re = 10^6, $G = 0.02$, and $C_w = 2500$ at different radial locations r^*.

4.2.2. Turbulence statistics

As for turbulent flows belonging to regime IV [1], turbulence is concentrated along the stator when an axial inward throughflow is superimposed (see Figure 25). Nevertheless, one characteristic feature of these flows compared to flows in large clearance cavities is that turbulence intensities decrease when one moves toward the periphery of the cavity. According to the maps of Re_t (see Figure 27), turbulence is enhanced by the inlet and the outlet of the axial throughflow. Besides, the maximum of turbulence is obtained in the outlet region close to the hub. This behavior is very similar to the one obtained in the case of a centrifugal throughflow, previously discussed.

The effect of the flowrate coefficient on the turbulent field is displayed in Figure 26. A centripetal throughflow increases the turbulent intensities and there is no threshold value for C_w contrary to the case of a centrifugal throughflow. If the flowrate coefficient is increased by a factor 2, turbulence levels increase by almost a factor 1.5. For a given Reynolds number Re = 10^6, the aspect ratio G = 0.02 and the radial location $r^* = 0.57$; by comparing the results shown in Figures 11, 19, and 26, the maximum of turbulence intensities is obtained along the stator when an inward throughflow is superimposed. Note that the values of the normal Reynolds stress tensor components are still quite comparable in the whole cavity.

The effect of an inward throughflow on the maps of the turbulence Reynolds number Re_t is highlighted in Figure 27. As in the case of an outward throughflow, the maximum values of Re_t are localized along the hub which corresponds to the outlet region of the flow. It is a combined effect of the rotating hub and of the outcoming jet, which creates a fully turbulent flow region at the lowest radii. A second flow region of high turbulence levels is found at the periphery of the cavity along the shroud and especially at the impact of the incoming flow with the stator. $\mathrm{Re}_{t_{\max}}$ is an increasing function of both Re and C_w but the influence of the flowrate coefficient remains larger in the present case.

Figure 28 presents the anisotropy invariant maps when an inward throughflow is superimposed on a turbulent torsional Couette flow (Re = 10^6 and $G = 0.02$) at two radii.

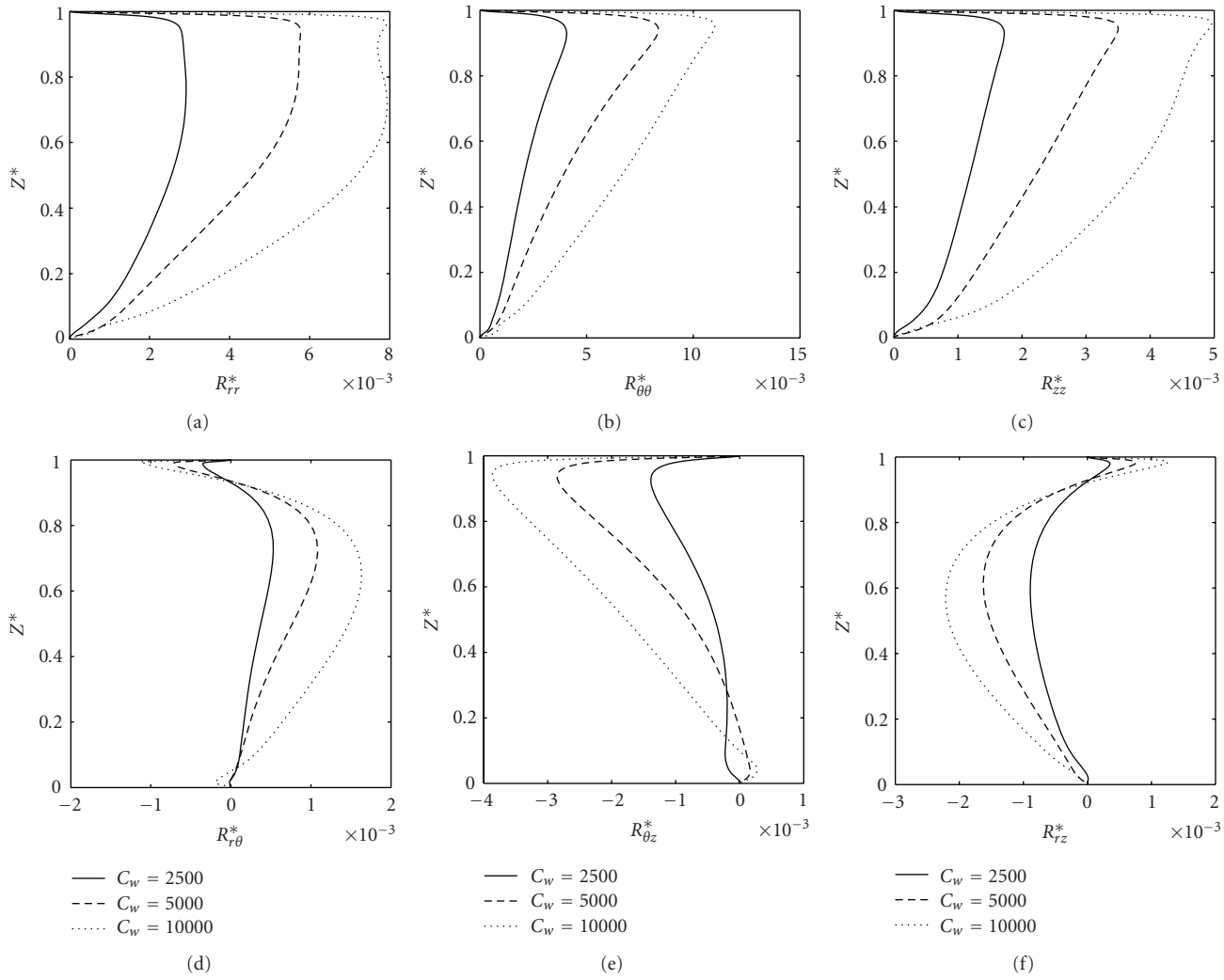

Figure 26: Axial profiles of the six Reynolds stress tensor components for Re $= 10^6$, $G = 0.02$ at $r^* = 0.57$ and three flowrate coefficients $C_w > 0$.

Turbulence tends to the one-component limit close to the disks and is fairly close to the isotropic case at midplane. The map remains almost the same whatever the values of C_w are and for these two radial locations.

5. CONCLUSION

New extensive numerical predictions using a second-order statistical modeling have been performed to describe the flow in a rotor-stator system of very small aspect ratio with or without throughflow according to a large range of the flow control parameters: the rotational Reynolds number $1.8 \times 10^5 \leq \text{Re} \leq 10^7$, the flow rate coefficient $-10^4 \leq C_w \leq 10^4$, and the aspect ratio of the cavity $0.02 \leq G \leq 0.05$.

In a closed cavity, depending on the parameters, the flow exhibits a torsional Couette flow structure with merged boundary layers for small clearances and a Batchelor structure with unmerged boundary layers for large ones. This study was mainly focused on regime III defined by Daily and Nece [1]; turbulent torsional Couette flows with merged boundary layers. The axial profiles of the mean tangential velocity in that case remain very similar to the ones obtained for Batchelor flows (regime IV). On the contrary, the profiles of the radial velocity are quite different. It is always linear in the main part of the flow as in classical plane Couette flows. Turbulence is almost homogeneous along the axial direction and vanishes toward the disks. When one moves from the axis of rotation to the periphery of the cavity, the boundary layers thicken and turbulence intensities increase as the local Reynolds number increases. Thus, for increasing values of the radius r^*, for a given set of parameters (Re, G), the successive transitions between regimes II and IV and then between regimes IV and III can be obtained in agreement with the scenario proposed by Cooper and Reshotko [9].

When an axial outward throughflow ($C_w < 0$) is superimposed on the main tangential flow, the flow structure switches to a Stewartson behavior for large values of $|C_w|$ or for small radii r^*, as in regime IV [2]. The tangential velocity is almost zero outside the region attached to the

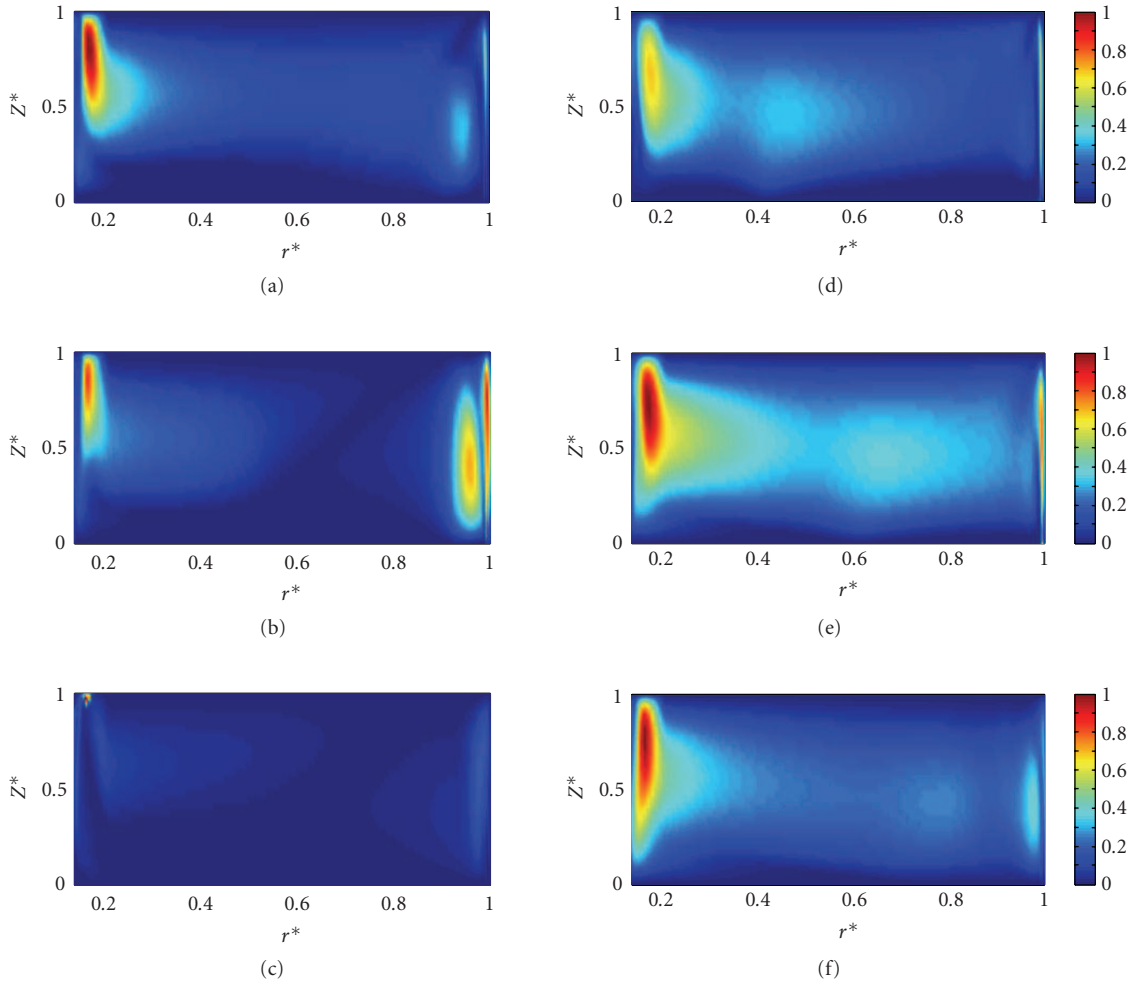

FIGURE 27: Isovalues of $\mathrm{Re}_t/\mathrm{Re}_{t_{\max}}$ for $G = 0.02$ and six sets (Re, C_w): (a) $(1.8 \times 10^5, 2500)$, $\mathrm{Re}_{t_{\max}} = 675.94$; (b) $(1.8 \times 10^5, 5000)$, $\mathrm{Re}_{t_{\max}} = 1557.5$; (c) $(1.8 \times 10^5, 10\,000)$, $\mathrm{Re}_{t_{\max}} = 4507.4$; (d) $(10^6, 2500)$, $\mathrm{Re}_{t_{\max}} = 1383.9$; (e) $(10^6, 5000)$, $\mathrm{Re}_{t_{\max}} = 1615.7$; (f) $(10^6, 10\,000)$, $\mathrm{Re}_{t_{\max}} = 3333$.

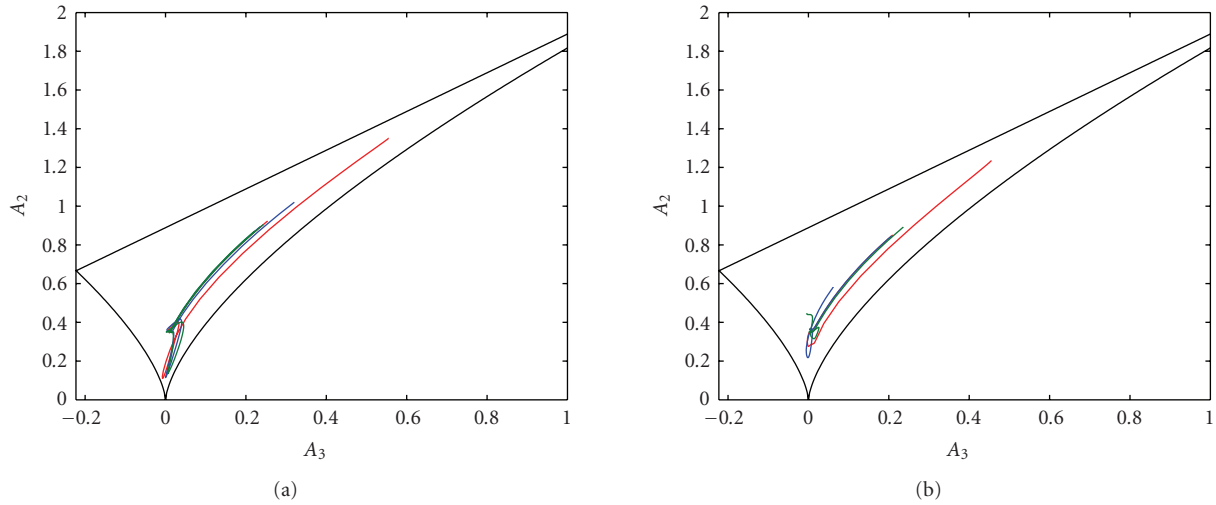

FIGURE 28: Anisotropy invariant map at (a) $r^* = 0.3$ and (b) $r^* = 0.7$ for $\mathrm{Re} = 10^6$, $G = 0.02$ and three flowrate coefficients: $C_w = 2500$ (red), $C_w = 5000$ (blue), and $C_w = 10\,000$ (green).

rotating disk and the radial velocity is positive everywhere. Turbulence is confined along the rotor and vanishes toward the stator. The maximum of the turbulence intensities is obtained at the inlet close to the rotation axis and turbulence levels slightly decrease when moving toward the periphery of the cavity.

In the case of an inward throughflow, the flow keeps the same characteristics than flows belonging to the regime IV. Depending on the flow control parameters, the fluid can rotate faster than the rotating disk because of the conservation of the angular momentum. The flow is then purely centripetal. It appears for large values of C_w or/and close to the rotation axis. Turbulence is mainly confined along the stator and vanishes toward the rotor. It is enhanced by the incoming axial jet.

The predictions of the present RSM turbulence model have been found here in good agreement with the velocity measurements performed at IRPHE. It strongly improves the predictions of the k-ϵ model of Launder and Sharma [27]. Nevertheless, more experimental data are now required, especially for the turbulent field, to enable more extensive comparisons and the improvement of the turbulence models.

NOMENCLATURE

a:	Radius of the hub, m
A_2, A_3:	Second and third invariants of the anisotropy tensor
b:	Outer radius of the rotating disk (m)
C_w:	Flowrate coefficient
G:	Aspect ratio of the cavity
h:	Interdisk spacing (m)
j_h:	Radial gap between the hub and the stator (m)
j_s:	Radial gap between the rotor and the shroud (m)
k:	Turbulence kinetic energy (m^2/s^2)
Q:	Volume flowrate (m^3/s)
r, θ, z:	Cylindrical coordinates (m)
R_m:	Curvature parameter of the cavity
Re:	Rotational Reynolds number based on b
Re_r:	Local Reynolds number based on r
Re_t:	Turbulence Reynolds number
R_{ij}:	Reynolds stress tensor with $i, j = (r, \theta, z)$ (m^2/s^2)
V_r, V_θ, V_z:	Radial, tangential, and axial velocity components (m/s)
ε:	Dissipation rate of the turbulence kinetic energy (m^2/s^3)
ν:	Kinematic viscosity of the fluid (m^2/s)
Ω:	Rotation rate of the rotating disk (rad/s)
Ψ:	Stream function
$*$:	Normalized quantity.

ACKNOWLEDGMENTS

The authors acknowledge Roland Schiestel (CNRS, IRPHE) for his fruitful discussions. The support for S. Haddadi by a Liebherr Aerospace grant is also acknowledged.

REFERENCES

[1] J. W. Daily and R. E. Nece, "Chamber dimension effects on induced flow and frictional resistance of enclosed rotating disks," *Journal of Basic Engineering*, vol. 82, pp. 217–232, 1960.

[2] S. Poncet, R. Schiestel, and M.-P. Chauve, "Centrifugal flow in a rotor-stator cavity," *Journal of Fluids Engineering*, vol. 127, no. 4, pp. 787–794, 2005.

[3] S. Poncet, M.-P. Chauve, and R. Schiestel, "Batchelor versus Stewartson flow structures in a rotor-stator cavity with throughflow," *Physics of Fluids*, vol. 17, no. 7, Article ID 075110, 15 pages, 2005.

[4] É. Séverac, S. Poncet, É. Serre, and M.-P. Chauve, "Large eddy simulation and measurements of turbulent enclosed rotor-stator flows," *Physics of Fluids*, vol. 19, no. 8, Article ID 085113, 17 pages, 2007.

[5] L. Schouveiler, P. Le Gal, and M.-P. Chauve, "Instabilities of the flow between a rotating and a stationary disk," *Journal of Fluid Mechanics*, vol. 443, pp. 329–350, 2001.

[6] J. M. Owen and R. H. Rogers, *Flow and Heat Transfer in Rotating-Disc Systems. Volume 1. Rotor-Stator Systems*, John Wiley & Sons, New York, NY, USA, 1989.

[7] J. W. Daily, W. D. Ernst, and V. V. Asbedian, "Enclosed rotating disks with superposed throughflow," Tech. Rep. 64, Department of Civil Engineering, Massachusetts Institute of Technology, Cambridge, Mass, USA, 1964.

[8] U. P. Phadke and J. M. Owen, "Aerodynamic aspects of the sealing of gas-turbine rotor-stator systems—part 1: the behavior of simple shrouded rotating-disk systems in a quiescent environment," *International Journal of Heat and Fluid Flow*, vol. 9, no. 2, pp. 98–105, 1988.

[9] P. Cooper and E. Reshotko, "Turbulent flow between a rotating disk and a parallel wall," *AIAA Journal*, vol. 13, no. 5, pp. 573–578, 1975.

[10] H. Iacovides and I. P. Theofanopoulos, "Turbulence modeling of axisymmetric flow inside rotating cavities," *International Journal of Heat and Fluid Flow*, vol. 12, no. 1, pp. 2–11, 1991.

[11] S. Poncet, *Écoulements de type rotor-stator soumis à un flux: de Batchelor à Stewartson*, Ph. D. thesis, Université Aix-Marseille I, Marseille, France, 2005.

[12] L. Elena and R. Schiestel, "Turbulence modeling of rotating confined flows," *International Journal of Heat and Fluid Flow*, vol. 17, no. 3, pp. 283–289, 1996.

[13] H. I. Andersson and M. Lygren, "LES of open rotor-stator flow," *International Journal of Heat and Fluid Flow*, vol. 27, no. 4, pp. 551–557, 2006.

[14] O. Czarny, H. Iacovides, and B. E. Launder, "Precessing vortex structures in turbulent flow within rotor-stator disc cavities," *Flow, Turbulence and Combustion*, vol. 69, no. 1, pp. 51–61, 2002.

[15] C. Cambon and L. Jacquin, "Spectral approach to non-isotropic turbulence subjected to rotation," *Journal of Fluid Mechanics*, vol. 202, pp. 295–317, 1989.

[16] L. Jacquin, O. Leuchter, C. Cambon, and J. Mathieu, "Homogeneous turbulence in the presence of rotation," *Journal of Fluid Mechanics*, vol. 220, pp. 1–52, 1990.

[17] B. E. Launder and D. P. Tselepidakis, "Application of a new second-moment closure to turbulent channel flow rotating in orthogonal mode," *International Journal of Heat and Fluid Flow*, vol. 15, no. 1, pp. 2–10, 1994.

[18] R. Schiestel and L. Elena, "Modeling of anisotropic turbulence in rapid rotation," *Aerospace Science and Technology*, vol. 1, no. 7, pp. 441–451, 1997.

[19] L. Elena, *Modélisation de la turbulence inhomogène en présence de rotation*, Ph. D. thesis, Université Aix-Marseille I-II, Marseille, France, 1994.

[20] B. J. Daly and F. H. Harlow, "Transport equations in turbulence," *Physics of Fluids*, vol. 13, no. 11, pp. 2634–2649, 1970.

[21] T. J. Craft, *Second-moment modelling of turbulent scalar transport*, Ph. D. thesis, University of Manchester, Manchester, UK, 1991.

[22] M. M. Gibson and B. E. Launder, "Ground effects on pressure fluctuations in the atmospheric boundary layer," *Journal of Fluid Mechanics*, vol. 86, no. 3, pp. 491–511, 1978.

[23] B. E. Launder and W. C. Reynolds, "Asymptotic near-wall stress dissipation rates in a turbulent flow," *Physics of Fluids*, vol. 26, no. 5, pp. 1157–1158, 1983.

[24] P. G. Huang and M. A. Leschziner, "Stabilization of recirculating flow computations performed with second moments closures and third order discretization," in *Proceedings of the 5th International Symposium on Turbulence and Shear Flow*, Cornell University, Ithaca, NY, USA, August 1985.

[25] S. Poncet and R. Schiestel, "Numerical modeling of heat transfer and fluid flow in rotor-stator cavities with throughflow," *International Journal of Heat and Mass Transfer*, vol. 50, no. 7-8, pp. 1528–1544, 2007.

[26] S. Poncet, R. Schiestel, and R. Monchaux, "Turbulence modeling of the Von Kármán flow: viscous and inertial stirrings," *International Journal of Heat and Fluid Flow*, vol. 29, no. 1, pp. 62–74, 2008.

[27] B. E. Launder and B. I. Sharma, "Application of the energy-dissipation model of turbulence to the calculation of flow near a spinning disc," *Letters in Heat and Mass Transfer*, vol. 1, no. 2, pp. 131–137, 1974.

[28] J. L. Lumley, "Computational modeling of turbulent flows," *Advances in Applied Mechanics*, vol. 18, pp. 123–176, 1978.